Materials
Horizons

REVIEW

View Article Online
View Journal | View Issue

Check for updates

Cite this: *Mater. Horiz.*, 2022, **9**, 220

Narrowband organic photodetectors – towards miniaturized, spectroscopic sensing

Yazhong Wang, † Jonas Kublitski, † Shen Xing, Felix Dollinger, Donato Spoltore, ‡ Johannes Benduhn * and Karl Leo*

Received 31st July 2021,
Accepted 23rd September 2021

DOI: 10.1039/d1mh01215k

rsc.li/materials-horizons

Omnipresent quality monitoring in food products, blood-oxygen measurement in lightweight conformal wrist bands, or data-driven automated industrial production: Innovation in many fields is being empowered by sensor technology. Specifically, organic photodetectors (OPDs) promise great advances due to their beneficial properties and low-cost production. Recent research has led to rapid improvement in all performance parameters of OPDs, which are now on-par or better than their inorganic counterparts, such as silicon or indium gallium arsenide photodetectors, in several aspects. In particular, it is possible to directly design OPDs for specific wavelengths. This makes expensive and bulky optical filters obsolete and allows for miniature detector devices. In this review, recent progress of such narrowband OPDs is systematically summarized covering all aspects from narrow-photo-absorbing materials to device architecture engineering. The recent challenges for narrowband OPDs, like achieving high responsivity, low dark current, high response speed, and good dynamic range are carefully addressed. Finally, application demonstrations covering broadband and narrowband OPDs are discussed. Importantly, several exciting research perspectives, which will stimulate further research on organic-semiconductor-based photodetectors, are pointed out at the very end of this review.

Introduction

Photodetectors (PDs), often also called photosensors, convert incoming optical signals into electrical signals and are widely employed for imaging,[1] medical diagnostics,[2,3] distance measuring,[4] optical signal communication, *etc.*[5] The current commercial market of PDs is dominated by crystalline

---

Dresden Integrated Center for Applied Physics and Photonic Materials (IAPP) and Institute for Applied Physics, Technische Universität Dresden, Nöthnitzer Str. 61, 01187 Dresden, Germany. E-mail: johannes.benduhn@tu-dresden.de, karl.leo@tu-dresden.de

† Contributed equally.

‡ Current address: Institute for Materials Research (IMO-IMOMEC), Hasselt University, Wetenschapspark 1, 3590 Diepenbeek, Belgium.

Yazhong Wang

Yazhong Wang received his master degree from Linköping University, Sweden in 2017. In October 2017, he joined Dresden Integrated Center for Applied Physics and Photonic Materials (IAPP) at Technische Universität Dresden as a PhD student under the supervision of Prof. Dr Karl Leo. His research interests fall on exploring organic electronics for near-infrared sensing applications from exploring new material combinations to designing novel device architectures.

Jonas Kublitski

Jonas Kublitski obtained his master degree at Paraná Federal University in Brazil. In 2016, he joined the group of Prof. Dr Karl Leo at the Dresden Integrated Center for Applied Physics and Photonic Materials, where he pursued his PhD. During this period, he worked on organic photodetectors (OPDs), investigating fundamental mechanisms, such as dark current generation and photomultiplication in narrowband devices. Currently, he is a postdoctoral fellow in the same group. His research topics go towards the development of new OPD structures, formation of trap states and their relation with noise current in optoelectronic devices as well as charge carrier transport.

inorganic devices, such as silicon (Si) or indium gallium arsenide (InGaAs) PDs. With the rapid development of the digital lifestyle, the demand for PDs is continuously increasing. For modern applications, lightweight, bio-compatible, and flexible PDs are promising candidates for realizing innovative products. However, intrinsic features of inorganic materials make it expensive or impossible to meet this demand. Organic semiconductors, on the other hand, are naturally compliant with such requirements.

Consequently, organic PDs (OPDs) have attracted much interest due to their advantageous features: OPDs are characterized by properties like lightweight, flexibility, low-cost, large-area scalability, and semi-transparency, making them potential candidates for the growing demand for smarter and safer sensors supporting daily life.[6–9] Regarding the device manufacturing, OPDs can be made by a multitude of technologies, including vacuum thermal evaporation, organic vapor phase deposition[10] or solution-based processes (spin coating, slot-die coating,[11] blade coating, spray coating,[12] inkjet printing, stamping,[13] roll to roll printing/lamination[14]). These approaches are much easier to implement than the advanced manufacturing techniques of inorganic PDs, including high temperature and complex lithography processes.[15] Furthermore, the chemical structures of photo-absorbing materials can be modified on the molecular scale, enabling a tunable photoresponse of OPDs, covering the electromagnetic spectrum from ultra-violet (UV) to near-infrared (NIR) light.[16–18]

Benefiting from advanced material synthesizing techniques, narrowband OPDs with many improved properties have been emerging in recent years,[19–23] with promising features like high selectivity of the target wavelength compared to broadband

Shen Xing

Shen Xing received her BS and MS degree from the University of Electronic Science and Technology of China (UESTC). In October 2017, she started her PhD under the supervision of Prof. Dr Karl Leo at the Dresden Integrated Center for Applied Physics and Photonic Materials at Technische Universität Dresden. Her current research interests focus on high-performing organic photodetectors (OPDs) achieved by newly developed device structures and fabrication methods, aiming to facilitate OPDs to advanced sensor applications.

Felix Dollinger

Felix Dollinger received his diploma and PhD in physics from Technische Universität Dresden in Germany. He is specialized in organic electronics and has previously published on organic solar cells as well as organic transistors. Recently he focuses on material development for organic photodetectors. One of his main research goals is the development of stable and sustainable organic electronic devices that will enable previously impossible applications.

Donato Spoltore

Donato Spoltore obtained his master degree at the University of L'Aquila (Italy) in 2009 and the PhD at the University of Hasselt (Belgium) in 2013. From 2014 to 2017 he was postdoc at the Technische Universität Dresden (Germany) and from 2018 to 2020 group leader of the organic solar cell group of the same university. Currently he is senior postdoc in the ERC project ConTROL at the University of Hasselt (Belgium). His research interests are centered on the fabrication, characterization, and understanding of fundamental processes in organic photovoltaic, photodetecting, and light-emitting devices.

Johannes Benduhn

Johannes Benduhn studied Physics at University of Greifswald (Germany), University of Wrocław (Poland), and Technische Universität Dresden (Germany), where he obtained his master (2015) and doctorate degree (2019) under the supervision of Prof. Koen Vandewal. Afterwards, he joined the start-up Senorics GmbH, which is expediting mobile spectroscopy solutions based on OPDs. Currently, Johannes Benduhn is leading the research group "Organic Sensors and Solar Cells" at Technische Universität Dresden under guidance of Prof. Karl Leo. His main research interests are ranging from studying fundamental processes in organic semiconductors to improving optoelectronic devices by employing new materials and exploring new device architectures.

counterparts. In addition, several elegant strategies were introduced to achieve narrowband OPDs, allowing to avoid synthetic variation of the photo-absorbing materials, such as charge collection narrowing (CCN),[24] charge injection narrowing (CIN),[25] self-filtering,[26] and microcavity enhanced narrowband OPDs.[27] All of these strategies are based on broadband absorbers often used in organic solar cells (OSCs). For OSCs, a high absorption coefficient and broad absorption range of the photo-absorbing materials are needed to harvest a large portion of the solar spectrum and gain large photocurrents. During the past years, the organic electronic community has seen a significant revolution with the development of non-fullerene acceptors (NFA), which led to an impressive improvement of the OSC power conversion efficiency to above 18%.[28–31] This new family of electron accepting materials with absorption edges up to 1100 nm[32] has great potential for both broadband and narrowband OPDs.

This review summarizes the recent progress, advancing strategies, challenges and potential applications of narrowband OPDs, ranging from materials to device architectures. We firstly introduce OPDs based on different operation mechanisms, mainly focusing on exploring and summarizing photovoltaic type OPDs (PV-OPDs). Additionally, organic photomultiplication devices (PM-OPDs) are discussed. Recent challenges of OPDs related to the key performance parameters such as responsivity (R), reverse dark current (J_D), response speed, dynamic range (DR), and linear dynamic range (LDR) are addressed as well. Afterwards, narrowband OPDs based on narrow-photo-absorbing materials and device architecture engineering are summarized and compared to broadband OPDs. Finally, we present an overview of potential applications and their demonstration, enabled by the advanced features of OPDs like lightweight, flexibility, large-area scalability, and semi-transparency. Examples include photoplethysmography, heart-beat monitoring sensors, NIR image sensors for visible-blind imaging, and miniaturized spectrometers for material analysis. We conclude with remarks on the status of narrowband OPDs and give a perspective for their future development.

Karl Leo

Karl Leo obtained the Diplomphysiker degree in 1985 and a PhD degree in 1988. From 1989 to 1991, he was postdoc at Bell Laboratories. From 1991 to 1993, he was with RWTH Aachen. Since 1993, he is full professor at TU Dresden. His main interests are novel semiconductor systems like semiconducting organic thin films. His work was recognized by a number of awards, including Leibniz-Award (2002), Zukunftspreis of the German President (2011), and Lifetime Inventor Award of the European Patent Office (2021). He is cofounder of several companies, including Novaled GmbH, Heliatek GmbH and Senorics GmbH.

Fundamentals of organic photodetectors (OPDs)

For interested readers, we summarized the performance metrics as well as their characterization in detail, which can be found in the appendix to this review.

Photodetection concepts of OPDs

Based on their principle of operation, OPDs can be classified into organic photoconductors (PC-OPDs), organic phototransistors (PT-OPDs), organic photomultiplication devices (PM-OPDs), and organic photodiodes or photovoltaic type OPDs (PV-OPDs) which are introduced below.

Organic photoconductors (PC-OPDs). Photoconductors profit from an intrinsic property of semiconductors, *i.e.* the photoconductivity, which is enhanced with increasing light intensity. Therefore, photoconductors are also called photoresistors. Incoming photons with energy larger than the optical gap (E_{opt}) of the involved photo-absorbing materials are absorbed and create free charge carriers, thereby increasing the electric conductivity of the active layer. As sketched in Fig. 1a, the simplest structure comprises two metallic contacts, separated by a distance L, and the photo-active layer in between, in a planar configuration. The electrodes are usually composed of the same material and form ohmic contacts with the active layer.[33] Due to the lack of built-in field as compared to photodiodes, PC-OPDs must be operated under external bias,[34,35] which can also assist free charge carrier generation.

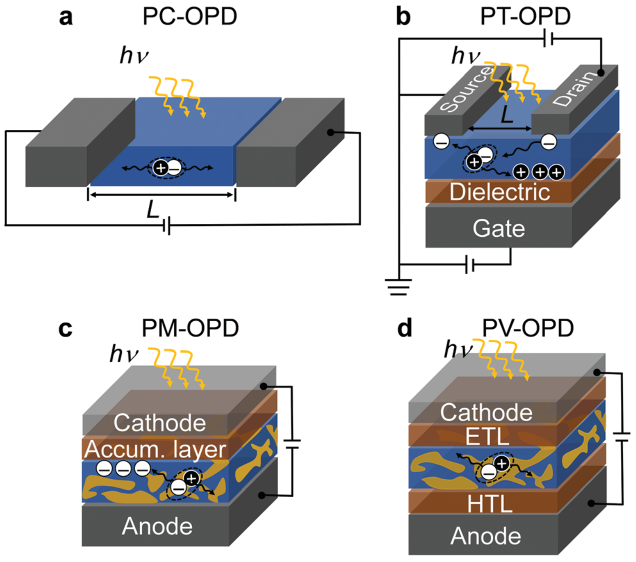

Fig. 1 Schematic of organic electronic device architectures for photodetection. (a) Organic photoconductor (PC-OPD); (b) organic phototransistor (PT-OPD); (c) photomultiplication type OPD (PM-OPD), in this example an accumulation (accum.) layer is inserted to block electrons; and (d) photovoltaic type OPD (PV-OPD) with an electron (ETL) and hole transport layer (HTL).

An attractive feature of PC-OPDs is the photoconductive gain (G), which can be exploited, for example, by means of unbalanced charge carrier mobilities. After exciton separation, the faster (majority) charge carrier type is extracted, while the slower one (minority) is still on its way. Within the lifetime of the minority charge carriers, majority carriers are injected by the external applied field; if the transit time of the majority charge carriers is shorter than the lifetime of the minority charge carriers, a G higher than unity is obtained.[36] This process runs until the minority charge carriers recombine; therefore, G is proportional to the lifetime of photogenerated species.[37] However, photoconductors typically suffer from high dark currents and slow response speed. While the high dark current is ascribed to the ohmic contacts formed between contacts and active layer,[38] the slow response speed is induced by the slow minority charge carrier mobility, often being holes.[39,40] In general, there is a compromise between G and response speed. The longer the lifetime of the minority charge carrier is, the more majority charge carriers pass through the device, but the slower the device becomes.

Organic phototransistors (PT-OPDs). Similar to organic field-effect transistors (OFETs), the architecture of PT-OPDs can be separated into three electrodes (gate, source and drain) and single photo-absorbing layer (channel). After being first introduced by Tsumura *et al.* in 1986 using polythiophene as the semiconductor layer,[41] PT-OPDs have been developed with mainly four different architectures: bottom-gate top-contact (Fig. 1b), bottom-gate bottom-contact, top-gate top-contact, and top-gate bottom-contact, to meet specific applications. Further information regarding device architectures are explained by Lucas *et al.*[42] The source–drain resistance of the blue-colored channel in Fig. 1b can be modulated by applying bias to the gate electrode. Furthermore, the applied bias can assist the charge-carrier separation and dissociation of the photogenerated electron–hole pairs in the channel with length L. By varying the gate bias, the charge-carrier density can be modulated, resulting in a high photoconductive gain. Therefore, the photocurrent of PT-OPDs can be enhanced, resulting in EQEs over 100%.[43]

Organic photomultiplication devices (PM-OPDs). Compared to their inorganic counterparts, avalanche photomultiplication, where one photogenerated charge carrier can induce several free carriers under high applied external electric field, cannot be achieved in OPDs: this is caused by the disordered nature and high exciton binding energy of organic materials.[44–46] Instead, a different principle was introduced by Hiramoto *et al.* in 1994.[47] Since then, PM-OPDs with photocurrent gain, achieved by trap-state-induced tunneling injection of charge carriers, were broadly investigated.[25,48–50] Similar to the previously described organic phototransistors, PM type OPDs can pave the way for improving the performance of traditional PDs under low light intensity or in low absorption wavelength regions (*e.g.* NIR). PM-OPDs can be realized by charge carrier trapping at the interface,[46,47,51–53] trapping centers,[54–57] and ultra-low acceptor (or donor) concentration.[25,58,59] Besides that, also traps in transport layers[60–62] and blocking layers[63,64] were utilized to achieve charge accumulation (see Fig. 1c). The buildup of charge carriers introduces a localized electric field which induces an interfacial energy level bending to assist tunneling injection of the opposite charge carrier type from the external circuit at reverse bias, resulting in PM photogain enhancement with an internal quantum efficiency (IQE) higher than 100%.[48,50,65] Meanwhile, low dark currents can be maintained due to the rectifying characteristics of these OPDs.

Photovoltaic type organic photodetectors (PV-OPDs). In general, OPDs are based on the photovoltaic effect to convert incident photons into an electric signal. Unlike OSCs which aim to achieve as high as possible power conversion efficiency, OPDs target on high photoresponse (R) and specific detectivity (D^*). Photogenerated excitons are dissociated at the interface between electron donating (D) and accepting (A) molecules, a D–A heterojunction, by forming charge-transfer (CT) state excitons. Afterwards, electrons and holes are transported to and extracted by the cathode and anode, respectively. It is worth noting that the mean free path of excitons in disordered organic materials is around 5–10 nm.[66,67] Therefore, the thickness of the photo-absorbing layer for a planar heterojunction (PHJ) is limited, suppressing the device photo-absorbing efficiency.[68] However, bulk heterojunctions (BHJs), formed by blending the donor and acceptor materials, can easily avoid this drawback.[69,70] Since an absorbed photon can generate at best one electron–hole pair, the EQE of PV-OPDs cannot surpass 100%. In conjugated organic semiconductor solids, photo-generated Frenkel excitons have large binding energies (0.3–1.0 eV),[71] which suppresses charge separation and results in a high probability of recombination. Therefore, most PV-OPDs are based on a photo-absorber with a D–A heterojunction configuration (Fig. 1d). Regarding the operating voltage, the detection mode of OPDs is generally divided into photovoltaic (PV) or self-powered mode at zero bias and extraction mode at reverse bias.

Introduction of broadband and narrowband OPDs

As far as spectral bandwidth is concerned, OPDs can be classified into broadband and narrowband OPDs. Broadband OPDs have high potential to be utilized for imaging,[1] medical diagnosing,[2,3] distance measuring,[4] optical signal communication, *etc.*[5] With the rapid development of organic semiconductor materials, the absorption range expands from ultra-violet (UV) and visible (Vis) to near infrared (NIR). In recent years, in the field of OSCs, organic materials with high absorption coefficient and broad absorption range are widely studied for harvesting a large part of the solar spectrum.[28–30] Such materials can also be sucessfully utilized for achieving broadband OPDs. Compared to their broadband counterparts, narrowband OPDs are endowed with higher performance for the mentioned applications like high-resolution imaging,[72] medical diagnosing under low light intensity,[50] material sensing, and light communication for specific target wavelength windows.[73] Moreover, narrowband OPDs with tunable wavelength feature can be employed to realize spectrometers with simple architecture, at low-cost and composed of non-heavy metals and harmless materials.[74,75] To realize narrowband detection, traditional inorganic broadband PDs are normally integrated with dichroic prisms, optical filters or gratings, having drawbacks such as complicated device architectures or limited pixel density of the image detecting array.[76–78] In the field of organic electronics, the following strategies have been explored to achieve narrowband detection without utilizing external devices:

- New molecular or polymeric materials with tailored narrowband absorption were synthetized.[20–22,72]
- In 2015, Armin *et al.* demonstrated the first red and NIR OPD with FWHM less than 100 nm. They realized CCN OPDs by using broadband-absorbing materials and a thick junction strategy.[24] In the same year, the group extended the concept to organohalide or mixed lead halide perovskites.[79]
- In 2017, tunable narrowband OPDs with BHJ embedded into Fabry–Pérot microcavities[80] were accomplished, with single or dual wavelengths detection capabilities.[27,74,81,82]
- In 2020, Xing *et al.* introduced self-filtering narrowband OPDs composed of a depletion layer, a donor and a thin acceptor layer, forming a planar heterojunction (PHJ).[83] Tunable red and NIR narrowband OPDs were achieved. Later, by manipulating exciton dissociation, narrowband OPDs with a hierarchical device architecture were demonstrated.[26,73]

The above introduced strategies to achieve narrowband OPDs mainly rely on PV-OPD and PM-OPD architectures and are explained in detail in the section Narrowband OPDs. There, we comprehensively summarize the design concepts, device architecture and the state-of-the-art of each approach. However, before that we are turning to recent challenges of OPDs since these challenges universally apply to broad- as well as narrowband OPDs.

Recent challenges for OPDs

In order to place OPDs as strong competitors to the current inorganic technology, OPDs need to achieve fast response speed and high D^*, which includes high mobility materials and increased on/off ratio, respectively. The D^* of PV-OPDs lies far below its background-limited infrared photodetection (BLIP) specific detectivity $\left(D^*_{\mathrm{BLIP}}\right)$, which corresponds to a perfect responsivity (EQE = 1 in eqn (9)) and noise current limited to the thermal generation of charge carriers over the optical gap of the material (i_{rad} in Fig. 2). While the former depends on several optoelectronic processes as summarized in Fig. 3a, the latter is mostly affected by the dark current of the device, which is orders of magnitude higher than its radiative limit. In what follows, a discussion about their state-of-art is given, in addition to an overview on the response speed, linearity and remaining challenges of OPDs to find broad commercial application. An overview of these challenges is given in Fig. 2 along with corresponding figures of merit.

High responsivity

For high responsivity (R), several optoelectronic processes must be optimized. These processes are summarized in Fig. 3a. A discussion about their state-of-art is given in the below.

Optical absorption. The first step to generate an electric output upon an optical input is absorption as sketched in

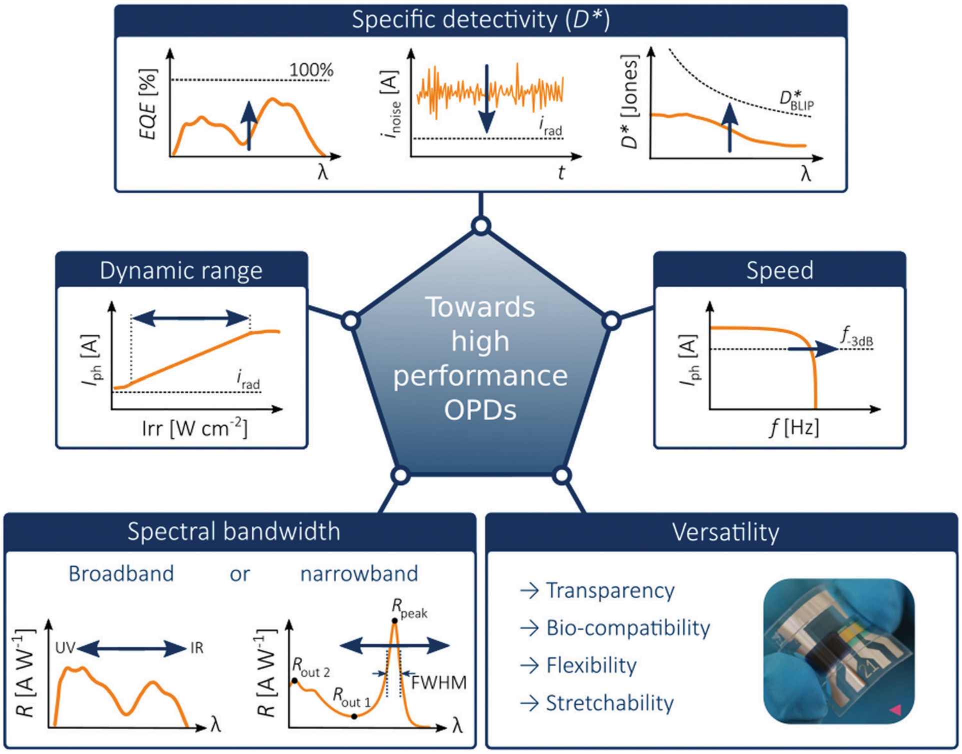

Fig. 2 Illustration of challenges for emerging OPDs. The picture of the flexible OPD is reproduced with permission,[27] copyright 2017, Springer Nature.

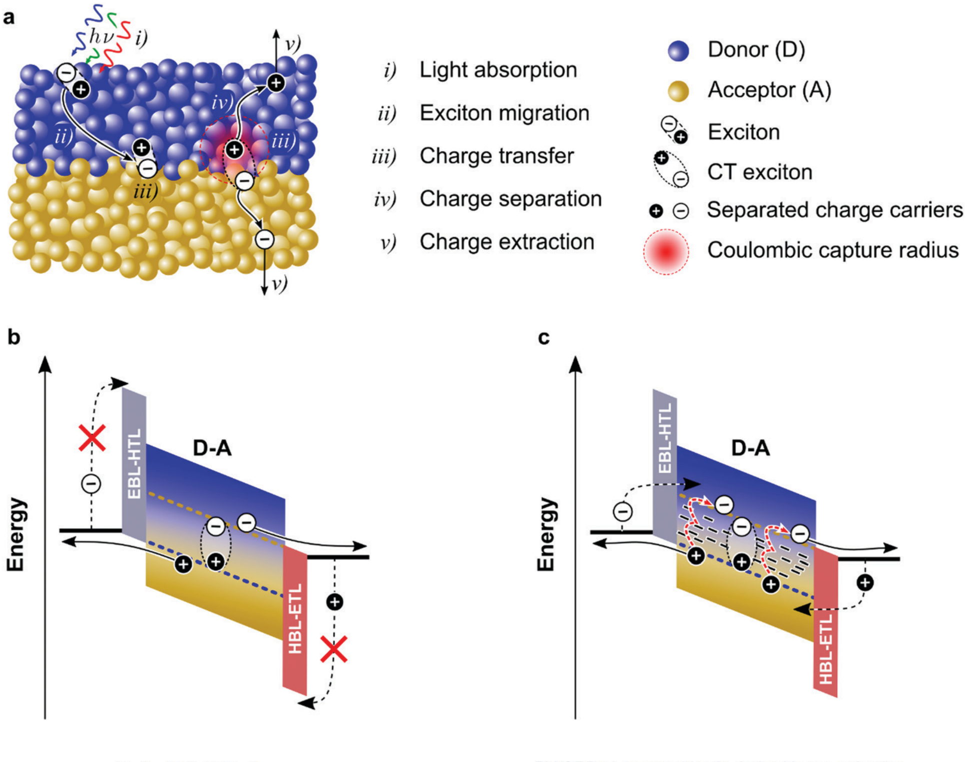

Perfect PV-OPD at reverse bias in dark

PV-OPD at reverse bias in dark with non-selective transport layers and charge-generating trap states

Fig. 3 Processes involved in photo and dark current generation. (a) Representation of a D–A layer demonstrating the steps from light absorption (i) to charge extraction (v). For simplicity, light absorption is represented only in the donor phase, while in fact the acceptor and CT states can also absorb light and follow the same steps. (b) Energetic sketch of a perfect PV-OPD at reverse bias where J_D is determined by J_0 due to the thermal generation of charge carriers over CT states. (c) Non-ideal OPD at reverse bias showing different sources of J_D, in addition to the ideal J_0: injection from the contacts as a result of poor or absent blocking layers and generation *via* trap states (shallow or deep).

Fig. 3a. Due to the strong overlap between the wave-function of the ground-state and first excited-state, the absorption of organic materials is usually strong. Additionally, the large geometrical relaxation of organic molecules in the excited state guarantees broad absorption peaks.[84] In general, the absorption is determined by the chemical structure of the material, where the incoming radiation interacts with the transition dipole moment of the molecule. Therefore, symmetric molecules, *i.e.*, with symmetry forbidden transitions, show low absorption. One example is the fullerene C_{60} and its soluble derivative, $PC_{61}BM$, which are among the most used acceptors in organic optoelectronic devices. These materials show the highest absorption up to 400 nm, leaving longer wavelengths to be mainly absorbed by the donor in the commonly used D–A structures.

Most recently introduced materials, including NFAs with strong absorption as compared to fullerenes, were designed to target the absorption of the solar spectrum. This reduces the amount of D–A systems to be employed beyond 1000 nm, and compromises the development of NIR and IR OPDs.[65,85] Additionally, OPDs generally contain transporting layers, which, as depicted in Fig. 3b and c, serve as selective and ohmic contacts. However, transporting layers also absorb light[86] but do not generate charge carriers, being therefore a source of photon losses.[87] Another source of losses refers to the Fresnel reflection at the semi-transparent electrode. Moreover, to achieve efficient charge dissociation, devices comprise nano-scale thin layers, which might not absorb the entire incoming radiation. Both issues have been addressed by optical manipulation such as light trapping.[88,89] Optical manipulation has also been used to increase the absorption in the CT state spectral region; using optical microcavities, CT-OPDs have been demonstrated, where not only the absorption is enhanced but also narrowband photoresponse is achieved.[27,74]

Exciton diffusion. Once light is absorbed, excitons, *i.e.* bound electron–hole pairs are generated. An efficient charge separation takes place at the interface between D and A. Therefore, within their lifetime excitons migrate a length L_D and should reach an interface where exciton dissociation takes place, see step (ii) in Fig. 3a. It has been shown that L_D for organic materials is in the order of 5–10 nm,[67,90–92] while the attenuation length for absorption amounts to around 50 nm, establishing a trade-off between light absorption and exciton dissociation, also compromising the use of PHJs.[93] In fact, J_{SC} of PHJs has a quasi-linear dependence on L_D.[94] To circumvent this trade-off, BHJs can be employed, where a D and A are mixed, forming separated domains; however, for efficient exciton quenching, such domains should be as large as L_D, which is difficult to achieve, since the control of the phase separation and the morphology is very challenging. Often, more than two phases are present, leading to higher recombination. Similarly to PHJs, in BHJs, J_{SC} was also shown to depend on the diffusion length L_D, which has been increased by increasing the film crystallinity.[95]

Generally, exciton migration is described by two types of energy transfer process: the Förster[96] and the Dexter[97] energy transfer. In the former, also called Förster resonance energy transfer (FRET), energy is transferred by the dipole–dipole coupling between the donating and the accepting molecule. The efficiency of this transfer decreases with increasing distance between molecules as r^{-6}, leading to a substantial contribution of FRET only within a D–A separation range of 1–5 nm.[98,99] Note that here D and A refer to molecules of same species. As a rule of thumb, the FRET process dominates the singlet-exciton diffusion, while the diffusion of triplet-exciton between non-phosphorescent molecules is restricted to Dexter energy transfer type.[67] The latter is a short-range interaction which depends on the overlap of the wave-function of donor and acceptor molecule and involves the physical exchange of an electron.

Assuming FRET as the main diffusion mechanism, L_D depends on:

(a) the dipole–dipole orientation
(b) the intermolecular distance
(c) the photoluminescence (PL) quantum yield
(d) the spectral overlap between the PL of the donor and absorption of the acceptor
(e) the refractive index and
(f) the ratio τ_f/τ_0, where τ_f is the PL lifetime limited by quenching defects and τ_0 is the intrinsic PL lifetime in the absence of defects.[100]

Besides being difficult to control, both (a) and (b) have a minor impact on the final L_D. Diminishing the non-radiative decay paths to increase the PL quantum yield (c) is expected to have a stronger influence on L_D. Highly ordered crystals are also expected to improve L_D. Lunt *et al.* showed that L_D increases from 6.5 nm in the amorphous film to 25 nm in single crystals, which is also connected to changes in the PL quantum yield.[101] Menke *et al.* showed that L_D increases by diluting the donor into a matrix consisting of a high-gap material, leading to decreased non-radiative decay rates.[93,102] By adding chemical side-groups to organic molecules, Raisys *et al.* increased the spectral overlap (d), thereby increasing L_D. Moreover, a lower refractive index (e) should lead to a larger L_D. Similarly to many properties of optoelectronic devices, traps (f) are detrimental for L_D. Indeed, Monte Carlo simulations indicate that traps are responsible for a major reduction of L_D.[103] A detailed discussion on exciton diffusion in organic solids can be found in ref. 67 and 93.

Charge-transfer and exciton dissociation. When an exciton reaches a D–A interface, a charge-transfer between D and A takes place, where an electron or hole are transferred to the A or D phase, respectively, see step (iii) in Fig. 3a. Electron transfer is known to be extremely fast, in the order of fs. Hole transfer was also shown to be very fast in D–A systems involving NFAs,[104] which is an important outcome, as NFAs are generally more absorbing than fullerene acceptors. Although a consensus about charge-transfer speed exists, the role of the so-called driving force, which represents the energy offset from the LUMO (HOMO) of the D to the LUMO (HOMO) of the A for electron (hole) transfer, has been controversially discussed.

According to Marcus theory, the electron transfer becomes more efficient as E_{CT} becomes lower than the optical gap of the D–A system.[105,106] In general, when using fullerenes as A, it is assumed that a driving force of about 0.1 eV is needed to assist efficient charge transfer,[107–109] while recently reported NFA systems show desirable performance at negligible driving force.[110,111] Nevertheless, as the energy offset E_{opt}–E_{CT} decreases, repopulation of the singlet states becomes more probable, whose decay rates are faster than those of the CT states, being therefore associated with reduced device performance.[112–115] In addition, some studies also suggest that if the triplet state on the D or A phase has a lower energy than E_{CT}, it can be an efficient path for recombination.[116] However, a further study indicates that fullerene triplets are responsible for recombination, whereas the D triplet states are inactive even though their energy is 300 meV lower than E_{CT}.[117] Moreover, it has been shown that triplets are not an active recombination path for non-geminate recombination.[118]

Another important discussion regarding CT states is which factors are decisive for efficient charge separation, see step (iv) in Fig. 3a. Because CT states are strongly bound,[119] overcoming the Coulomb energy barrier is necessary to release free carriers. At room temperature, thermal energy is not sufficient to assist this transition and the question about how bound CT states get split arises. It has been proposed that higher-energy CT states are responsible for efficient free charge generation, while the yield provided by the relaxed ones would be low. The role of the so-called ''hot CTs'' has been intensively debated and a final conclusion is yet lacking. From a generation yield close to 100%, it has been shown that regardless of the excitation energy, IQE remains constant, down to photonenergies of E_{CT}.[120] Moreover, several groups have shown similar results from different perspectives, where no effects of the energy excess has been observed. However, different conclusions arise when considering ultrafast spectroscopy results.[121] Experimental data suggests that higher-energy CT states are faster in generating free charges. In one study, an increase in photocurrent was observed when additional infrared pulses were applied to steady-state illumination.[122] While experimental and theoretical studies point to the effect of higher-energy CT states,[123] data obtained by other groups contradict those findings.[124]

Charge transport and collection. After exciton separation, free charge carriers are driven to the electrodes due to the built-in field (OPDs in self-powered mode) or by an additionally applied reverse bias (OPDs in extraction mode), see step (v) in Fig. 3a. The efficiency of this event depends mainly on the charge carrier mobility of the material. With unusual exceptions for highly ordered materials,[125–128] organic compounds show a modest mobility in the range of 10^{-6}–10^{-2} $\mathrm{cm^2\,V^{-1}\,s^{-1}}$, strongly dependent on processing conditions. The weak electronic coupling between molecules, the strong disorder and large electron-vibration coupling hinders the formation of electronic bands and causes localized charge carriers in different energetic sites. While there is consensus that charge transport in such disordered molecular solids happens *via* thermally activated hopping, polaronic effects are also believed to affect the mobility.[129] Additionally, charge trapping at water clusters[130] or by lattice disorder[131] has been suggested to slow down charge transport. Here, the tradeoff between PHJs and BHJs is met as well as a compromise between light absorption (thick active layers) and efficient charge collection (thin active layers). While PHJs deliver a better charge transport, BHJs show better exciton separation and light absorption.

Low dark current

Dark current – fundamentals. The most important operation regime for OPDs is under reverse bias, in which charge carriers are extracted more easily due to the applied electric field. Additionally, read-out circuits usually operate under bias, making it difficult to keep the OPD at zero volts (self-powered mode) in real applications. Therefore, achieving a low reverse dark current (J_D) is essential for the future development of OPDs, since reaching low J_D translates into higher D^*.

The lower limit of J_D in any PV-OPD is determined by the dark saturation current, J_0, in addition to the diffusion current.[37] J_0 arises from thermal generation of charge carriers over the states at which thermal equilibrium is achieved and is, therefore, unavoidable. For inorganic semiconductors, such states define the band gap, usually leading to low intrinsic dark currents. For organic semiconductors, however, the charge generation within single materials is rather poor, which was circumvented by the introduction of HJs formed between D and A. The charge-carrier generation happens at intermolecular CT states, whose energy E_{CT} is lower than the optical gap of the single materials. In dark at zero bias, equilibrium between thermal generation and recombination is achieved *via* CT states. As sketched in Fig. 3b, when a negative bias is applied, thermally generated charges are extracted, causing J_0 to be determined by the CT states properties:[132,133]

$$J_0 \approx \frac{q}{\mathrm{EQE_{EL}}} f_{\mathrm{CT}} \frac{2\pi}{h^3 c^2} (E_{\mathrm{CT}} - \lambda_{\mathrm{CT}}) \exp\left(-\frac{E_{\mathrm{CT}}}{k_B T}\right), \quad (1)$$

where $\mathrm{EQE_{EL}}$ is the external quantum efficiency for electroluminescence, λ_{CT} the reorganization energy of the CT state, and f_{CT} is proportional to the oscillator strength of the CT transition and the density of CT states. A similar scenario is observed at open-circuit voltage (V_{oc}), where no net current flows. Here, photogenerated charge carriers recombine *via* CT states. In fact, J_0 and V_{oc} are related by:

$$V_{\mathrm{oc}} \approx \frac{k_B T}{q} \ln\left(\frac{J_{\mathrm{sc}}}{J_0}\right), \text{ for } V_{\mathrm{oc}} \gg \frac{k_B T}{q}, \quad (2)$$

where J_{sc} is the diode short-circuit current. The relation between V_{oc} and CT states properties has been demonstrated from various perspectives.[134,135] However, observing a decreasing J_D with increasing E_{CT} is not as straightforward due to many extrinsic parameters that dominate the measured J_D,[136–138] see Fig. 3c. In fact, J_D of most OPDs reported in literature lies far above its lower limit, J_0.

In the field of OSCs, one of the recently broadly discussed topics is the origin of non-radiative voltage losses, which are much higher than in inorganic solar cells, and hence, limit the maximum achievable power conversion efficiency.[135,139] It is worth noting that this discussion is also valid for OPDs, where non-radiative losses lead to higher J_0 as predicted by a lower $\mathrm{EQE_{EL}}$ in eqn (1). While the majority of the OPDs are still far above the non-radiative limit, in NIR absorbing devices non-radiative paths tend to become the major source of dark current.[138] Different strategies have been reported for the reduction of extrinsic dark currents and are summarized below.

Dark current reduction. For a long time, the deviation of J_D from its intrinsic limit was mainly attributed to injection due to the poor selectivity of the contacts. Therefore, most approaches developed to reduce J_D focused on raising the energy barrier for injection under reverse bias targeting a better selectivity of the contacts, which can be achieved *via* blocking layers[140] and the use of the PHJ structure.[141,142] Another strategy to increase the selectivity of the contacts is making use of phase segregation in mixed D–A systems, such that a pure phase of D and A is maintained at the anode and the cathode, respectively.[143,144] It is worth mentioning that PHJs lead to a reduced interfacial area and a lower density of CT states (N_{CT}), which also reduces J_D and increases V_{oc},[134] as N_{CT} is included in the parameter f_{CT} in eqn (1).[132] In fact, care must be taken when comparing J_D of the same D–A system (when D and A form different phases, are used at different concentrations or are employed in PHJs), since all these specificities might lead to quite different CT state properties, which ultimately defines the lower limit of J_D.

Aiming to increase the injection barrier at reverse bias meanwhile forming ohmic contact at forward bias, it is common to use layers that re-define the Fermi alignment of the contact. The most known material system for solution-processed devices is PEDOT:PSS for hole injection.[145] For electron injection, different materials are employed, such as PEIE[146,147] and ZnO nanoparticles.[148] In vacuum-processed devices, ohmic contacts are generally achieved by molecular doping of electron-transporting layers (ETL) and hole-transporting layers (HTL),[86] which also work as blocking layers in reverse bias for the opposite charge carrier type. While employing doped layers is a reliable solution to achieve selective contacts, it has been shown that lateral leakage currents arise from these layers, requiring device engineering to minimize this problem.[149]

Another issue is related to the roughness of the rather omnipresent ITO transparent contact. Spikes much higher than the average thickness of the layer resulting from patterning methods can lead to ohmic shunt paths, increasing J_D. The problem can be circumvented by utilizing smoothing polymeric layers or increasing the thickness of the active layer.[74,150–152]

Dark current investigation and modeling. Despite several strategies developed to reduce the dark current of OPDs, the measured value strongly differs from that predicted by eqn (1). This discrepancy indicates that the source of J_D is likely related to material characteristics, rather than device engineering. With that in mind, a few studies were performed to investigate the origin of the high dark currents in optimized devices, for which the strategies to reduce J_D were shown to be less effective.

Intra-gap trap states are generally detrimental for the operation of optoelectronic devices. Besides the known effects on charge carrier mobility, increased recombination rates, and reduced L_D, an increase of J_D has also been attributed to traps, see Fig. 3c. Dark and photocurrent of OSCs were described according to the model proposed by Hurkx *et al.* for inorganic semiconductors,[153,154] where the generation rate is increased by the tunneling of trapped charge carriers into the band. The model is a modified version of the Shockley-Read-Hall (SRH) theory. Assuming a Gaussian distribution of deep traps and SRH generation rates, Fallahpour *et al.* modeled the dark current of OPDs for the P3HT:PC$_{61}$BM blend, even though the field dependence was not studied. The authors also discussed that injection from the contacts cannot explain the high J_D.[155] Recently, Kublitski *et al.* showed that J_D is proportional to the experimentally measured amount of mid-gap traps and their characteristics. In the same work, J_D was described by a field-assisted de-trapping model based on Poole–Frenkel effect, which explains the magnitude and field dependence of the experimental results.[136] Moreover, the presence of mid-gap states was suggested to increase J_0, re-defining the thermodynamic limit of organic solar cells and OPDs.[156]

Nonetheless, Simone *et al.* attributed the high J_D and its activation energy to the injection of charge carriers from the contacts into the band tails of different polymers.[157] Similarly, Zarrabi *et al.* suggested that band tails are the source of J_D due to thermal generation over the reduced tail-to-tail optical gap.[156] A better understanding of the extrinsic dark currents and their reduction will remain a key subject of research in the coming years.

Speed

The response speed of PV-OPDs can be limited by the RC time of the measurement setup (sheet resistance of the device, contact resistance and load resistance of the equipment), by the transit time of the slowest carrier or both as described by eqn (19).[158] Therefore, strategies to increase the response speed in this class of devices target one or both of the limiting cases. On the one hand, reduced RC time can be achieved by employing smaller devices with reduced sheet resistance and, ideally, thick undoped layers. On the other hand, increasing the device thickness leads to an increased transit time τ_{tr}, which is undesired. τ_{tr} is determined mainly by the charge carrier mobility, therefore, the same trade-offs apply as discussed for charge collection.

Saggar *et al.* showed that the response speed of PTNT:PC$_{71}$BM (50 wt%) is limited by the slow electron transport as compared to the hole transport.[159] By increasing the PC$_{71}$BM concentration, the electron mobility was increased and the hole mobility slightly decreased. The balanced charge carrier mobilities led to an increase in the cutoff frequency, as shown in Fig. 4a. In the same direction of intentionally tuning transport properties, Ullbrich *et al.* fabricated devices comprising varying active areas, in order to study the intrinsic response speed (not RC limited) of narrowband CT-OPDs.[160] The authors observed an increasing response speed upon decreasing active area due to the reduced capacitance (RC limit). The response speed saturates at 8 ns (0.07 nF), where the low hole mobility of the ZnPc donor limits the response speed. By engineering a planar-mixed (D/D–A/A) structure, the authors controlled the transit path for holes and electrons while keeping the device and active layer (D–A) thickness constant (see Fig. 4b). This approach led to a record cutoff frequency of 68 MHz as depicted in Fig. 4c.

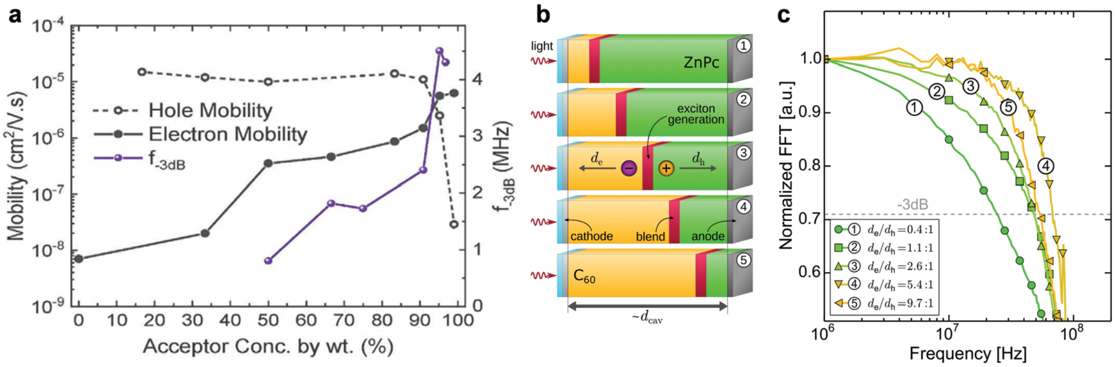

Fig. 4 (a) PTNT:PC$_{71}$BM blend-ratio impacts electron and hole mobilities along with the f_{-3dB} of OPDs. The balanced charge mobility occurs at the PC$_{71}$BM concentration of ∼95%, for which the largest f_{-3dB} values (4.5 MHz) is achieved. (b) Simplified device architectures of the planar-mixed heterojunction cavity enhanced OPDs. Neat layers of ZnPc (donor) and C$_{60}$ (acceptor) are depicted in green and orange, respectively. Excitons are generated and dissociated into free charge carriers at the interface colored in red. (c) Modulated frequency response of OPDs sketched in (b). With shortening the slower carrier (hole) travel distance by reducing the thickness of ZnPc layer, the cutoff frequency rises (① → ④) to the maximum value of 68 MHz. Panel (a) is reproduced with permission.[159] Copyright 2021, Wiley-VCH GmbH. Panel (b) and (c) are reproduced with permission.[160] Copyright 2017, American Chemical Society.

In PM-OPDs, the response speed depends on the lifetime of trapped charges. Therefore, these devices are usually slower than PV-OPDs.[36,161] The fastest PM-OPDs operate in the range of kHz,[49] in contrast to the MHz range achieved by PV-OPDs. The response speed of PM-OPDs has been shown to increase with the applied voltage, which was attributed to a faster trap filling at the organic/metal interface.[162] Likewise, employing organic crystals leads to a fast accumulation, increasing the response speed,[163] which is also observed when a high negative bias is applied to devices comprising amorphous layers.[59] An intuitive overview on the response speed of PM-OPDs is given in ref. 161.

Dynamic range

A large DR is required to precisely detect signal of various intensities. Whether the device operates in the linear or sublinear regime depends on the photophysics of charge carrier dynamics in the device. For PV-OPDs, non-linear photoresponse is generally observed at high light intensities, which is mostly attributed to non-geminate, bimolecular recombination.[164] At high light intensities, a large amount of charge carriers accumulates at the D–A interfaces, increasing the probability of recombination and resulting in a reduced diffusion current. This effect becomes more pronounced if thick layers with low charge carrier mobility are involved.[165] Poor extraction was further correlated with increased bimolecular recombination.[166] In fact, it was shown that both non- and geminate recombination can be suppressed in devices with optimized morphology, which leads to an enhanced and field independent extraction.[167,168]

Nonetheless, recent theoretical simulation by Hartnagel *et al.* predicted that recombination *via* trap states as well as spatial charge effects in thick devices can also lead to sublinear photoresponse at high light intensities. In the same study, the authors suggested that sublinear deviations at low light intensities are caused by exponential band tails.[169]

Further challenges

Integration with circuit read out. For the development of imagers, for example, arrays of OPDs integrated with read out circuits are necessary. This can be done either by integrating OPDs with state-of-art CMOS technology or building completely organic based imagers, which is more challenging, as also organic transistors are required. Although some examples are found in the literature in that direction,[1,170–173] further research is needed.

High performance in the infrared spectral range. The demand for PDs extends further into the infrared region. Beyond 2500 nm, in the region currently covered by HgCdTe PDs, PV-OPDs have so far not been demonstrated.[138] In fact, it has been suggested by Gielen *et al.* that intrinsic limitations of organic materials will preclude the operation of PV-OPDs in the spectral region above 2000 nm.[138] Nonetheless, Vella *et al.* achieved D^* of around 10^9 Jones in the long-wave infrared region up to ≈ 12 μm using PC-OPDs.[35]

Flexible, stretchable, and biocompatible devices. For certain applications, the special mechanical properties of organic devices offer key advantages. However, only few examples can be found, where OPDs were built on flexible and/or stretchable substrates.[6,8,27,174] Additionally, OPDs are suitable for health/healing monitoring. Such applications could reduce the number of surgical interventions, provide precise dosing of medication and early diagnosis, among many other applications. However, depending on the region of use, biocompatible and biodegradable devices/materials are required. Research on OPDs suitable for these applications is a promising field for further research.

Narrowband OPDs

Traditional approaches for narrowband detection

Since decades, broadband inorganic PDs are state-of-the-art and different semiconductors cover a very broad range of the electromagnetic spectrum and achieve high D^*. Nevertheless, it has been challenging to achieve monolithic, narrowband inorganic PDs and therefore other approaches have been chosen to realize color-discrimination for broadband detectors.

Optical filters such as shortpass, longpass, and bandpass filters can be utilized to restrict the photoresponsivity of PDs such that only the intended wavelength range is detected. Such concepts are applied in CMOS- or CCD-based cameras where the color discrimination into the three primary colors is achieved usually by filters, utilizing the same semiconducting material for absorbing different colors. These detector-arrays are nowadays highly integrated and miniaturized, but still expensive. Additionally, the color selectivity is quite limited and different approaches are needed to achieve a spectroscopic resolution. Finally, the use of filters obviously generates losses.

For higher wavelength-resolution, typically, optically **dispersive elements** such as gratings (diffraction on a grating) or prisms (refraction in dispersive materials) are utilized to spatially decompose colors. Subsequently, the dispersed light is either detected by a line-detector, comprised by many individual PDs, or by selecting the relevant wavelength *via* an aperture such as slits in monochromator setups combined with a single broadband PD. In the latter configuration, the dispersive element is typically rotated to change the desired wavelength. Both of these approaches are highly performant and are the basis for scientific spectroscopy. Nevertheless, some of the intrinsic properties of the used components make such sensor systems rather large and expensive. For accurate detection of the separated wavelengths, the calibration of the dispersive elements is essential which is sensitive to environmental changes (*e.g.* temperature, vibrations). Additionally, line detectors are expensive, have limited lateral resolution and are sensitive to higher diffraction order of grating, restricting the detection range. All of these reasons lead to the fact that spectrometers are still quite expensive and, due to their fragile properties, mainly employed in laboratory environments.

Narrowband absorber materials

The spectral response of OPDs is correlated to the photo-absorbing layer (typically a D–A HJ), whose materials can be commonly classified into polymers and small molecules. By tailoring the molecular electronic structure, the absorption of new absorber materials can be sharpened for achieving narrowband OPDs. Both D and A materials have intrinsic photo-absorbing properties, which induce a broadened absorption of PHJ or BHJ systems. Hence, further strategies need to be employed to suppress the broad absorption. Emerging single-component systems have found to be promising in this regard. As shown in Table 1, PSQ[19] and ISQ[20] are a donor–acceptor–donor (D–A–D) single-component systems with a FWHM down to 110 nm and 80 nm and competitive D^* up to 7.7×10^{12} and 3.2×10^{12} Jones, respectively. In Table 1, figures-of-merit and recent years progress of narrowband OPDs with employing narrow-photo-absorbing materials are summarized. The normalized EQE of some OPDs based on typical narrow bandgap absorbers are shown in Fig. 5. It is notable that narrowband OPDs are still suffering from lack of narrow-photo-absorbing materials with small optical gaps.[175,176] Moreover, within this strategy, it is difficult to avoid a photoresponse outside the targeted detection window induced by the intrinsic absorption of photo-absorbing materials. In recent years, several advanced strategies were presented to realize narrowband OPDs, apart from chemical engineering of the absorber layer, which are presented below.

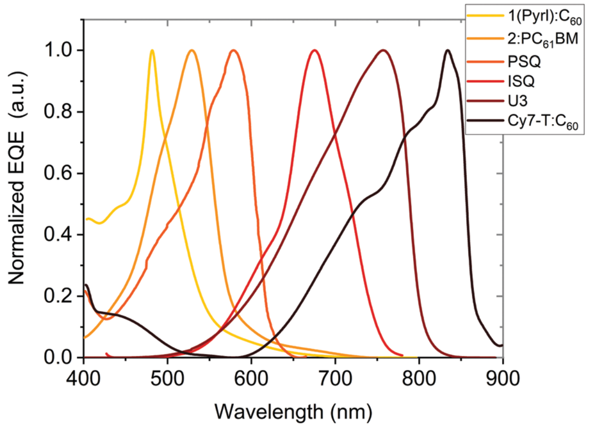

Fig. 5 Normalized EQE of OPDs based on narrow-photo-absorbing materials as a function of wavelength. 1(Pyrl):C_{60}[177] and Cy7-T:C_{60}[22] are PHJs. 2:$PC_{61}BM$[21] is a BHJ blend. PSQ[19] and ISQ[20] are single-component photo-absorbing materials with D–A–D chemical structure and U3 is also single component device.[23]

Charge collection narrowing (CCN)

Armin *et al.* introduced an interesting concept to achieve narrowband detection by manipulating charge collection efficiency in devices comprising thick active layers.[24] In this structure, incoming photons with energy above the optical gap (case A and B in Fig. 6a) are absorbed close to the transparent electrode. Holes photogenerated close to the anode (ITO) have a shorter transit time than that of photogenerated electrons, which must cross the entire thick layer. Hence, a space charge region arises, which screens the electric field responsible for the extraction, hindering charge collection. Therefore, electrons and holes in this region recombine. Incoming photons with energy near or slightly lower than the optical gap (case C in Fig. 6a), penetrate the device, reaching the back reflecting electrode. These photons create an interference effect such that generation happens in the entire bulk. In the ideal case, no space charge region is formed and both charge carrier types are efficiently extracted. In the photoresponse spectra, the balanced extraction is translated as a peak

Table 1 Figures-of-merit and progress of narrowband OPDs based on narrow-photo-absorbing materials. The numbers highlighted in italics were not given in the original publication and are here calculated/estimated based on other correlated data provided in the respective publication

Photo-absorbing materials	Peak [nm]	FWHM [nm]	D^* [Jones]	EQE [%]	R [A W^{-1}]	Bias [V]	LDR [dB]	f_{-3dB} [kHz]	Year	Ref.
Solution processing										
3:$PC_{61}BM$	500	130	—	8.2	*0.03*	−1.0	—	—	2013	178
2:$PC_{61}BM$	525	80	1.00×10^{11}	15.0	*0.06*	−1.0	80	25.0	2014	21
Cy7-T:C_{60}	850	100	1.00×10^{12}	17.0	0.12	−1.0	—	—	2015	22
1(Pyrl):C_{60}	481	76	2.00×10^{11}	18.0	0.07	0	—	—	2019	177
PolyTPD:SBDTIC	740	141	1.42×10^{13}	10.5	*0.06*	0	78	118.0	2019	179
PCZ-Th-DPP	709	170	4.63×10^{12}	—	—	−1.0	109	1.2	2019	180
PCbisDPP:$PC_{61}BM$	730	210	4.73×10^{11}	80.0	0.31	−3.0	—	—	2019	181
PCPDTBT:ZnO	725	175	—	68.0	0.40	—	—	—	2020	182
PSBOTz:PNDBO	530	155	1.10×10^{13}	*16.4*	0.07	−2.0	—	—	2020	183
1(Pyrl):1(Hex):C_{60}	754	11	1.10×10^{10}	14	0.086	0	61	150.0	2021	184
Vacuum processing										
DMQA:SubPc	586	131	2.34×10^{12}	60.1	0.27	−5.0	—	—	2013	185
SubNc	690	180	—	80.0	*0.45*	−15.0	—	—	2015	186
DM-2,9-DMQA:SubPc	580	115	2.03×10^{12}	56.5	0.26	−3.0	—	76.7	2014	187
ISQ	680	80	3.2×10^{12}	15.0	—	−2.0	114	190.0	2016	20
Rubrene:C_{60}	470	80	—	55.0	*0.21*	−1.0	—	86.0	2016	188
M1:C_{60}	550	67	3.73×10^{13}	59.0	*0.26*	−3.0	—	—	2016	72
PSQ	600	110	7.70×10^{12}	66.0	*0.32*	−2.5	96	—	2017	19
CiInPc:C_{60}	705	190	3.30×10^{12}	80.0	*0.45*	−1.0	77	2.9	2019	189
1a:C_{60}	560	97	4.37×10^{13}	70.0	*0.32*	−3.0	—	—	2019	190
SubPc:C_{60}	600	70	7.50×10^{11}	16.0	0.08	−1.0	—	—	2021	191

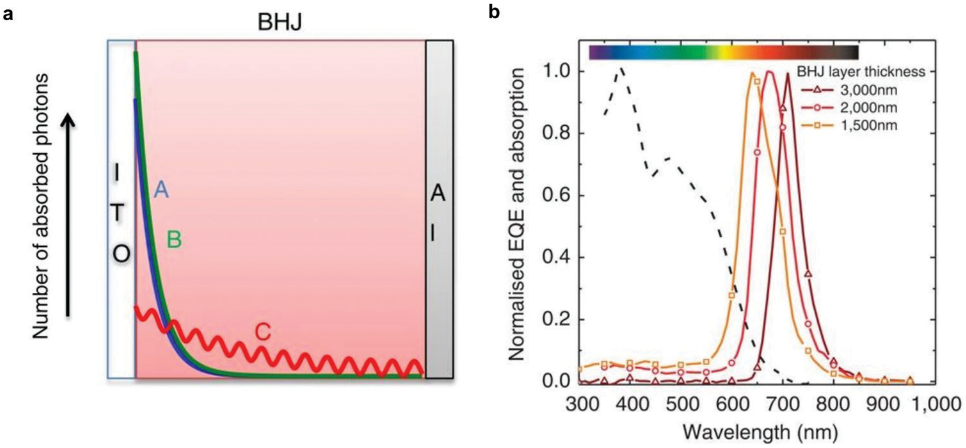

Fig. 6 Working principle and narrowband response of CCN-OPDs. (a) The structure of the CCN-OPD is shown with the absorbed photon distribution for selected wavelengths (A–C). (b) Normalized EQE spectra of the CCN-OPD with three different active layer thicknesses. Reproduced with permission.[24] Copyright 2015, Springer Nature.

located at the absorption onset of the active layer. By varying the active layer thickness, one can tune the position of the peak, as shown in Fig. 6b. The authors were able to apply the CCN concept to two material systems, PCDTBT:$PC_{71}BM$ and DPP-DTT:$PC_{71}BM$, leading to a NIR (shown in Fig. 6b) and red photoresponse, respectively. These devices reached D^* on the order of 10^{11} Jones.

The disadvantage of this approach is that micrometer-thick devices are required, which should have an optical density $\alpha l \gg 1$ (assuming $\alpha \approx 10^5$ cm^{-1} for organic materials), where α and l are the absorption coefficient of the active layer and the device thickness, respectively. This issue was circumvented by the same group by using inverted devices comprising unbalanced mobilities.[192] In this structure, only photons with energy close to the absorption onset generate holes that can be extracted, since they are close to the anode. Photons with energy above the optical gap generate slow holes close to the cathode. These holes cannot reach the anode and, therefore, recombine. With this approach, the thickness of the active layer was reduced to 700 nm, in contrast to the micrometer range previously required, and D^* on the order of 10^{13} Jones was demonstrated at 700 nm response wavelength.[192]

Charge injection narrowing (CIN)

Charge injection narrowing (CIN) was introduced by Wang *et al.*[25] and shares similarities with the concept of CCN discussed above. CIN combines the idea of CCN with photomultiplication, in order to achieve a narrowband spectral response with bias-enhanced EQE. The idea behind the spectral narrowing is the same; however, the active layer comprises a low-acceptor content, as previously reported for PM-OPDs.[161] Therefore, electrons generated near the cathode by photons with energy close to the absorption onset of the D–A system accumulate due to the reduced percolation paths. The accumulation leads to an energy level bending under applied reverse bias, triggering enhanced hole injection caused only by spectrally selected wavelengths.

The concept was also applied to achieve a dual band device which works as a conventional broadband PM-OPD when illuminated from the top and a narrowband CIN-PM-OPD when illuminated from the bottom, as shown in Fig. 7.[193]

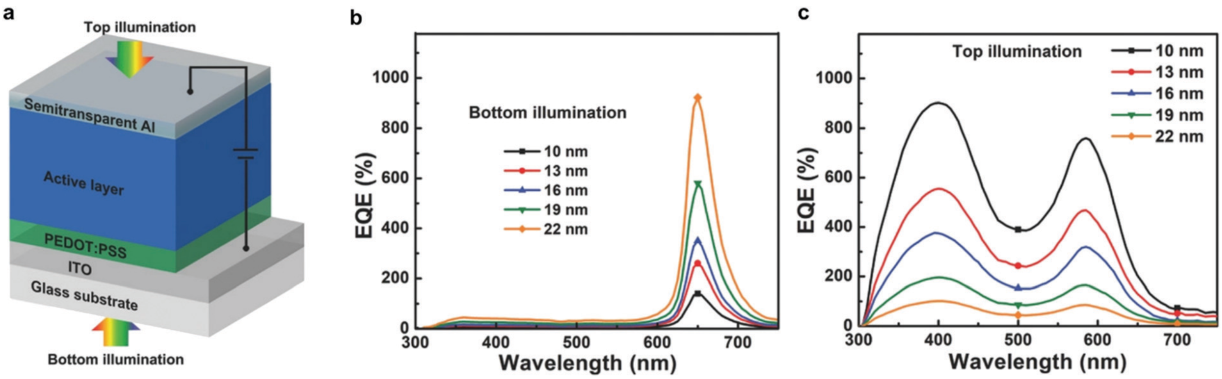

Fig. 7 (a) CIN-PM-OPD structure. EQE of the CIN-PM-OPD under (b) bottom and (c) top illumination. Reproduced with permission.[193] Copyright 2018, Wiley-VCH GmbH.

Interestingly, since the interference depends on the reflection of the incoming photons, when illuminated from the bottom and operated as a CIN-PM-OPD, the devices become more efficient with increasing top electrode thickness. Oppositely, when illuminated from the top and operated as a conventional PM-OPD, devices become less efficient with increasing the top electrode thickness due to the reduced incoming light. Both operation regimes lead to D^* in the range of 10^{11} Jones.

Self-filtering narrowband OPDs

Self-filtering narrowband OPDs have been proposed as a promising strategy in recent years to achieve narrowband photodetection. The large binding energy and small diffusion length of photogenerated Frenkel excitons are viewed as a significant drawback of organic semiconductors. However, this property offers the potential to achieve self-filtering narrowband OPDs with the help of a hierarchical device structure where thick larger optical gap donor layers are followed by a lower optical gap acceptor layer. Excitons generated by high-energy photons in donor front layers fail to separate into free charges. Only low-energy photons with a long penetration depth can reach the D–A interface and generate free charges for collection. Compared to the CCN method, thinner devices can be realized with high response speed and simple fabrication methods.

Xing *et al.* reported this device principle with a simple organic PHJ architecture that enables selective activation of excitons for tuning the photoresponse spectra.[83] The schematic device structure is shown in Fig. 8a. By adjusting the ratio of PTB7 in P3HT, an improved responsivity and red-shifted photoresponse peak from 645 to 745 nm were demonstrated simultaneously (Fig. 8b). The truly filterless device exhibited D^* above 10^{12} Jones with a narrow FWHM of around 50 nm. Concomitantly, Xie *et al.* proposed the same principle to manipulate the dissociation of Frenkel excitons intentionally.[26] The basic

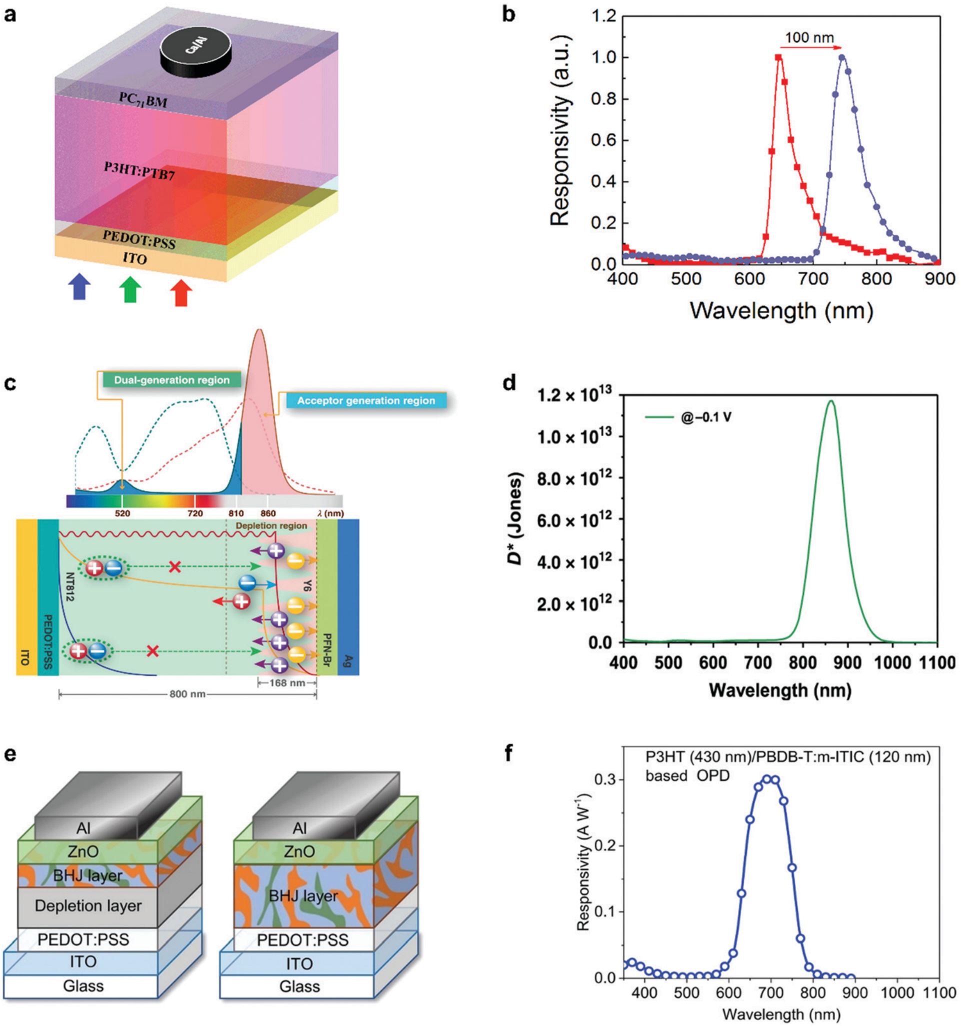

Fig. 8 Working principle and the narrowband response of self-filtering OPDs. (a) Device structure and (b) the tunability of normalized response peak of red-light OPDs.[83] (c) Working mechanism and (d) specific detectivity spectra (obtained from the dark current density) of self-filtering narrowband OPDs.[26] (e) Device structures and (f) responsivity spectrum under zero bias for the filter-free band-selective OPDs. Panel (a) and (b) are reproduced with permission.[83] Copyright 2020, American Chemical Society. Panel (c) and (d) are reproduced with permission.[26] Copyright 2020, Nature Publishing Group. Panel (e) and (f) are reproduced with permission.[73] Copyright 2020, Wiley-VCH GmbH.

device architecture and working mechanism are displayed in Fig. 8c. Due to the exciton dissociation narrowing, the filter-free narrowband OPD was accomplished, showing a peak EQE of around 65% at 860 nm with a FWHM of around 50 nm. Meanwhile, D^* over 10^{13} Jones was demonstrated (Fig. 8d). This device was one the best performing gainless type narrowband OPDs ever reported, with performance comparable to commercial Si PDs. Similarly, Lan *et al.* fabricated narrowband OPDs with a heterostructured photoactive layer comprising a depletion layer and a BHJ layer (Fig. 8e).[73] It was found that a 430 nm thick P3HT depletion layer combined with a 120 nm thick PBDB-T:m-ITIC BHJ absorbed the incident light for wavelengths smaller than 600 nm and gave a photoresponse in the deep-red region (Fig. 8f). Moreover, this work presented an inspiring option for application in de-multiplexing light communication.

Microcavity enhanced narrowband OPDs

In the past years, Fabry–Pérot microcavity-based[80] organic electronic devices have been demonstrated as a versatile methodology to realize narrowband OPDs with enhanced performance. Such resonance cavity enhanced OPDs are endowed with broad wavelength-range tunability and high selectivity. Moreover, the enhanced optical field within the cavity can also improve the total absorption of the photo-absorbing layer, resulting in enhanced spectral response at the resonance wavelength. Within the resonance cavity rejected wavelength range, the OPD has a much lower photoresponse than that of the resonance wavelength, leading to a high spectral rejection ratio (SRR), which indicates a good signal specificity. The tunability of the resonance wavelength can be easily realized by varying the thickness of layers within the cavity, allowing to build compact and highly integrated spectrometers without synthesizing new organic semiconductors for each wavelength.

Single-wavelength mode

Physics of microcavities. In general, the intrinsic absorption coefficient (α) at peak wavelength of typical photo-absorbing materials is around 10^5 cm^{-1},[82,85,194] which gives an absorption attenuation length of around 50 nm. Therefore, in normal organic electronic devices, such as OSCs, the needed photo-absorbing layer thicknesses are several tens to one hundred nanometers to achieve as high as possible absorption. In a cavity enhanced narrowband OPD, the effective absorption coefficient α_{eff} can be approximated by eqn (3). Compared to the photo-absorbing material, the absorption coefficient of interlayers and reflecting electrodes are neglected for this approximation.

$$\alpha_{\text{eff}} \approx \frac{\alpha l}{L}, \tag{3}$$

where l and L are the photo-absorbing layer thickness and cavity length, respectively. The FWHM is proportional to α_{eff} and L, expressed in eqn (4) and (5). The resonance wavelength λ_{m} solely depends on L and the refractive index (n) of the cavity. Where m = 1, 2, 3... represents the resonance order, and for $m > 1$, higher order resonance overtones appear.

$$\text{FWHM} \approx \frac{\alpha_{\text{eff}} \lambda_m{}^2}{n\pi}. \tag{4}$$

$$\lambda_m = \frac{2nL}{m}. \tag{5}$$

Utilizing above-gap absorption. To achieve OPDs with a small FWHM by employing photo-absorbing materials that are normally designed with high intrinsic α, the thickness of the photo-absorbing layer needs to be much thinner as compared to OSCs. Wang *et al.* fabricated cavity enhanced OPDs with a photo-absorbing layer thickness in the nanometer scale.[81] As shown in Fig. 9, tunable narrowband OPDs with a detection window covering the visible wavelength range were realized by using only 3 and 6 nm thick photo-absorbing layers. The resonance wavelength was tuned by varying the thickness of the microcavity, realized by varying the thickness of ETL and HTL simultaneously to ensure that the photo-absorbing layer is located in the optimized electromagnetic field, at which the cavity enhancement reaches the highest value. In Fig. 9b, the FWHM values of the OPDs were ranging between 28 and 43 nm in second order resonance (m = 2). By increasing the cavity thickness, the third order resonance (m = 3) was achieved, decreasing the FWHM to 25 nm with a resonance wavelength peak at 630 nm and 25% EQE. Even if the thickness of the photo-absorbing layer was only a few nanometers, the OPDs achieved a shunt resistance as high as 1 MΩ cm^2, leading to a specific detectivity over 10^{12} Jones.

Utilizing intermolecular CT state absorption. Dramatic efforts have been performed to synthesize organic semiconductor materials with narrow optical gap to extend the OPDs detection wavelength range into the NIR.[22,184] New materials rarely give a reasonable photoresponse beyond 1100 nm.[4,16,195] Additionally, it is challenging to achieve high detectivity in the NIR range by employing a materials with a narrow optical gap, which suffer from high noise current at zero external bias.[37,196] In 2017, Siegmund *et al.* introduced a promising method to achieve narrowband NIR OPDs by inserting a D–A BHJ inside a microcavity (Fig. 10a), utilizing thermal evaporation.[27] With blending D and A materials, intermolecular CT states are formed, featuring optical transitions below the D and A optical gaps (Fig. 10b). In general, the absorption coefficient of CT states is less than 10^3 cm^{-1} and continually declines with increasing wavelength. Therefore, the photoresponse induced by CT absorption is rather weak. The cavity enhances the absorption caused by intramolecular CT states and consequently a useful absorption well below the D and A optical gap is made possible. As shown in Fig. 10c, an EQE enhancement at CT absorption wavelength range up to 41-fold was achieved, with EQEs exceeding 20% and FWHM down to 36 nm. The narrowband NIR detection with wavelength tunability ranges from 810 nm to 1100 nm. Using an analogous strategy and employing a donor with a high HOMO level, D8, blended together with C_{60}, Kaiser *et al.* realized cavity enhanced

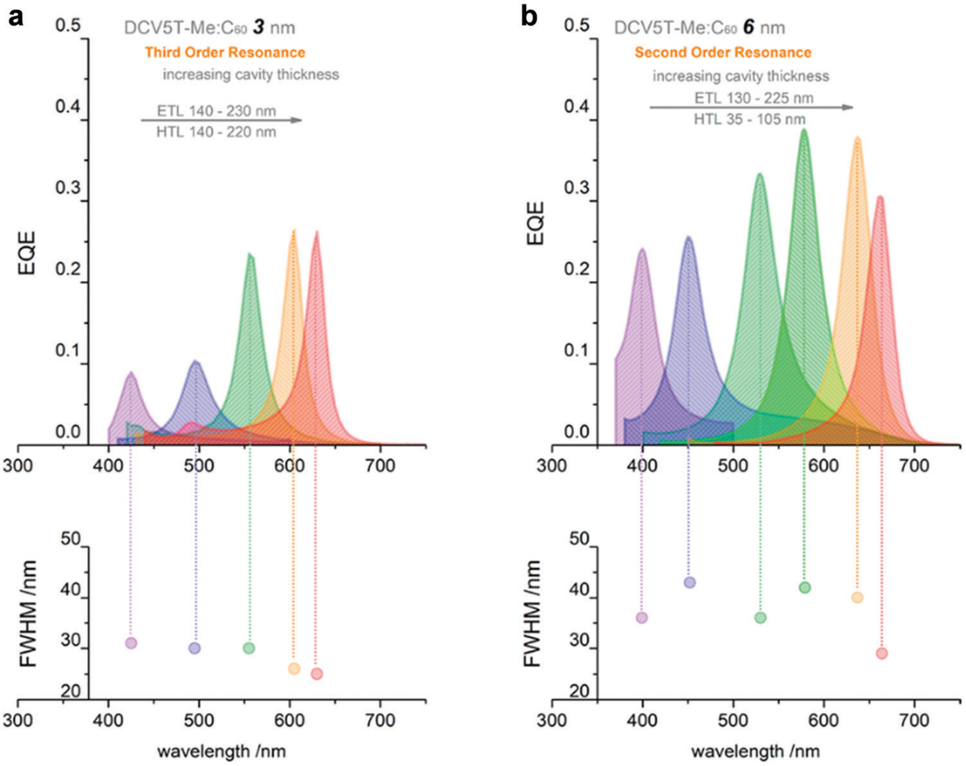

Fig. 9 EQE curves and correlated FWHM of cavity enhanced OPDs with (a) 3 nm thick photo-absorbing layer and third order resonance (m = 3) and (b) 6 nm thick photo-absorbing layer and second order resonance (m = 2). The tunable enhanced wavelengths are realized by varying the thickness of ETL and HTL. Reproduced with permission.[81] Copyright 2019, American Chemical Society.

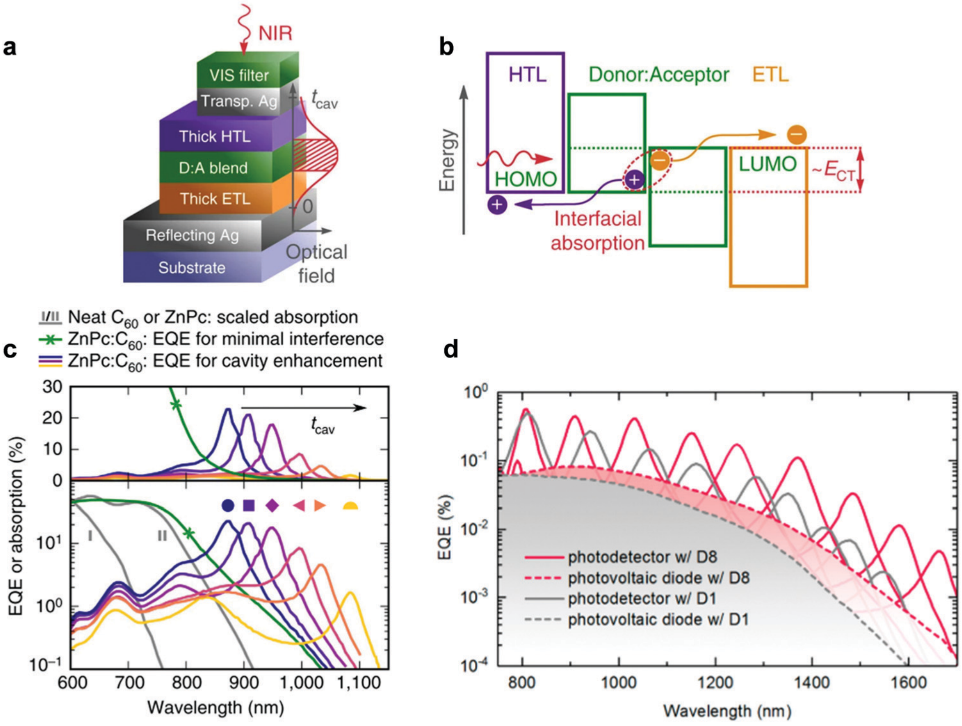

Fig. 10 (a) Simplified device architecture of a microcavity enhanced narrowband NIR OPD. (b) Schematic energy level diagram of the main materials involved in the OPDs. (c) NIR OPDs based on ZnPc:C_{60} CT state absorption. (d) NIR OPDs based on the CT absorption of D8:C_{60}. Subfigures (a–c) are reproduced with permission.[27] Copyright 2017, Springer Nature. Subfigure (d) is reproduced with permission.[197] Copyright 2019, American Chemical Society.

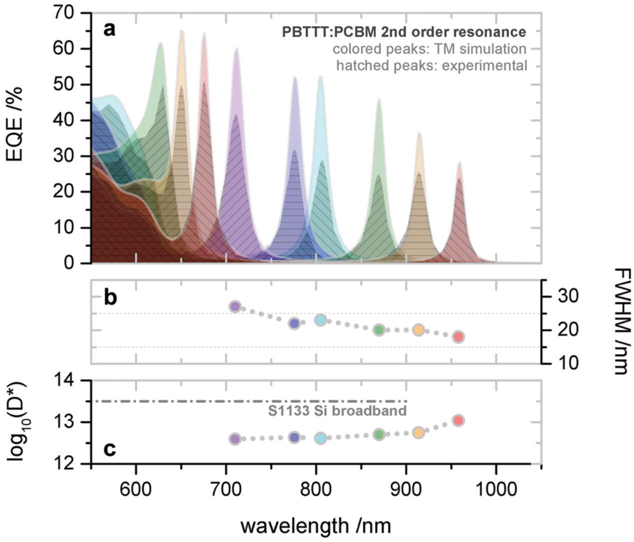

Fig. 11 Solution processed PBTTT:PC$_{61}$BM CT-OPDs based on the second order resonance. (a) Simulated and experimental (hatched) resonance wavelength and correlated EQE curves. The wavelength tunability in range of 650–910 nm was realized by varying the active layer thickness from 290–440 nm. (b) Corresponding FWHM and (c) *D**. Reproduced with permission.[74] Copyright 2017, WILEY-VCH GmbH.

narrowband NIR OPDs based on CT absorption with tunability covering the NIR from 810 to 1665 nm, and achieving a *D** at 1665 nm as high as 3×10^8 Jones.[197] Based on the work of Siegmund *et al.*, Mischok *et al.* combined a highly reflective distributed Bragg reflector (DBR) with a thin metal resulting in a sharp Tamm plasmon-polariton resonance. Compared with non-DBR devices, the performance of NIR OPDs based on CT absorption improved impressively, showing enhanced EQE up to 17% at a wavelength of 880 nm with FWHM down to 20 nm.[198]

Later on, the group also realized microcavity enhanced CT absorption narrowband NIR OPDs by solution processing.[74] With varying the thickness of the active layer (PBTTT:PC$_{61}$BM) from 290 nm to 440 nm, the second order resonance was achieved with EQE enhancement up to 40% at wavelength 720 nm (Fig. 11a) and FWHM (Fig. 11b) down to 20 nm at wavelength 910 nm. Benefiting from the thick active layer, the OPDs showed extraordinarily low dark current, resulting in *D** up to 10^{13} Jones (Fig. 11c), which is comparable to state-of-the-art silicon PDs. To extend the response further into the NIR, the authors employed PDPPTDTPT:SdiCNPBI as active layer demonstrating narrowband OPDs operating at wavelengths up to 1700 nm. Furthermore, Tang *et al.* also integrated several of these CT-OPDs with varying active layer thickness on a single substrate and thereby realized a miniaturized spectrometer, see Fig. 19a. As a showcase, the transmittance spectrum of water was reproduced, detailed information is supplied in the section: Potential application of narrowband OPDs.[74]

Multiple-wavelength mode. An elegant solution to realize OPDs which can distinguish several wavelengths *via* a single detecting surface were introduced recently.[199,200] Importantly, the accuracy of substance identification can be improved with the number of detected wavelengths. In 2020, Wang *et al.* demonstrated dual-wavelength narrowband NIR OPDs by stacking two sub-cavities on top of each other.[82] As shown in Fig. 12a, the ultra-compact OPD was constructed by inserting two photo-absorbing layers, ZnPc:C$_{60}$ and D6:C$_{60}$, in between three terminals, thus forming two sub-microcavities. ZnPc:C$_{60}$ and D6:C$_{60}$ sub-cells were utilized to detect optical signals in short and longer NIR wavelength ranges, respectively.

The tunability of each sub-cell was realized by varying the thickness of the photo-absorbing layer in one sub-cell, while keeping the other constant. As shown in Fig. 12b, the photoresponses of the thickness-varied sub-cell are tuned and those of the thickness-constant sub-cell remain constant (with negligible fluctuation). The tunable resonance wavelengths of the D6:C$_{60}$ sub-cell were covering 1020–1435 nm (D6:C$_{60}$ sub-cell). It is worth noting that the FWHM of the sub-cells was reduced to 61 nm. For the ZnPc:C$_{60}$ sub-cell, a response wavelength of 790–1180 nm and an FWHM down to 35 nm could be achieved.[82] As an application demonstration, the OPDs were utilized to determine ethanol concentration in a water solution by selecting a combination of two wavelengths corresponding to specific absorption bands from both liquids.

Microcavity enhanced narrowband PM-OPDs. Although the intrinsic amplification offered by microcavities is attractive, the EQE is limited by the low absorption cross section of CT states. A novel approach introduced by Kublitski *et al.*[201] integrates PM-OPDs into microcavities in order to overcome this limit. For this purpose, the authors fabricated vacuum-processed PM-OPDs based on reduced percolation paths due to the low acceptor concentration in ZnPc:C$_{60}$ (3 wt%) blends. The 400 nm thick PM-OPD was analyzed under operation in the CT state absorption region and showed a superior EQE compared to that of PV-OPDs comprising both 3 wt% and the optimized 50 wt%, commonly used for OSCs. At −10 V, IQE as high as 1750% was achieved in the range from 400 nm to 1200 nm for the broadband device. Embedding this structure within semitransparent mirrors as described above led to narrowband PM-OPDs as shown in Fig. 13a, with performance superior to that of comparable OPDs. Importantly, the narrowband PM-OPDs operate in the photomultiplication mode even in the CT absorption region, which could be verified by IQEs in the order of 900% at −15 V. Besides achieving *D** in the order of 10^{11} Jones as depicted in Fig. 13b, these devices reached cutoff frequencies as high as 19 kHz.

Combining microcavities with PM-OPDs represents a promising path to improve the sensitivity of CT-OPDs, since the benefits from the core properties of both devices can be combined. Nonetheless, narrowband PM-OPDs share the same drawbacks of PC-OPDs, which include generally higher J_D and low response speed as compared to PV-OPDs. However, a clear understanding of these properties is still missing.

Challenges for narrowband detection

As described previously, to realize monolithic narrowband OPDs, many different methods have been utilized such as synthesizing materials with narrowband absorption[19–21,23]

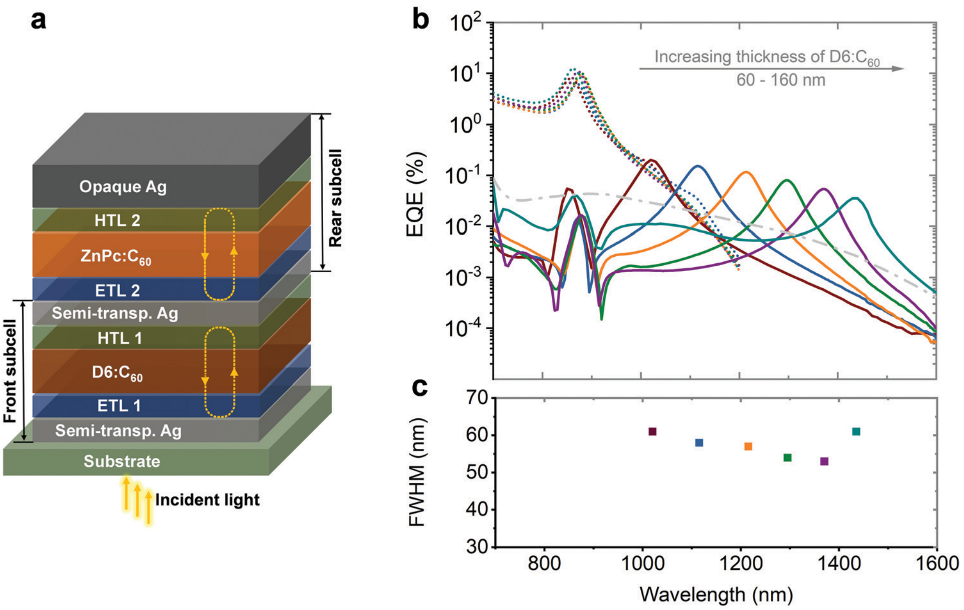

Fig. 12 (a) Simplified device architecture of the microcavity enhanced stacked dual-wavelength narrowband NIR OPDs based on CT state absorption. (b) EQE curves and correlated FWHM of the NIR OPDs. The wavelength tunability was realized by varying the thickness of the photo-absorbing layer in one sub-cell while keeping the other constant. The thickness of D6:C_{60} was varied from 60 to 160 nm, resulting in a tunable wavelength covering the 1020–1435 nm range (solid lines). The EQE of the other subcell (ZnPc:C_{60}) only changes negligibly (dashed lines). (c) The FWHM of each device are depicted in the lower panel. Licensed under CC BY 4.0.[82]

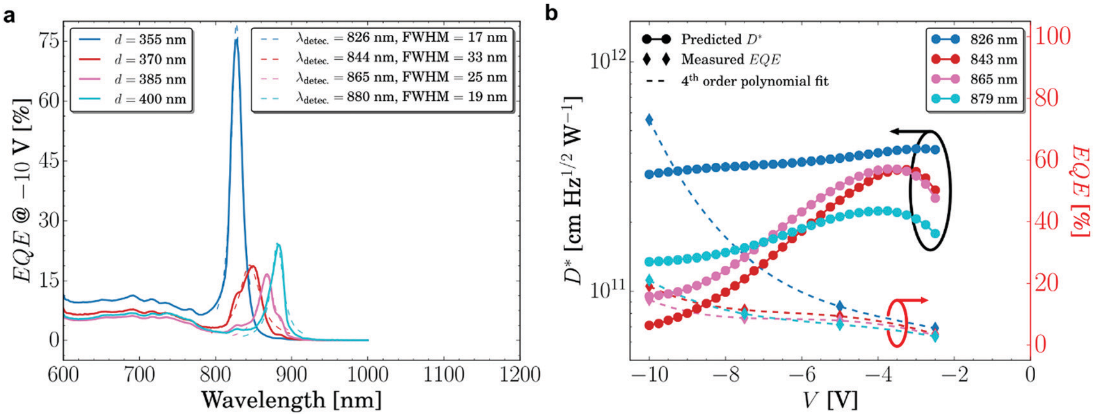

Fig. 13 (a) Amplified EQE of narrowband CT-PM-OPD at four resonance wavelengths at −10 V. (b) EQE and D^* of the same devices shown in (a) at various voltages.[201] Licensed under CC BY 4.0.

and developing novel device architectures *e.g.* CCN,[24] CIN,[25] and self-filtering OPDs.[26] However, by employing these methods, each material system can only supply one specific detection window, lacking an easy possibility for tuning the peak response wavelength. Furthermore, to manipulate the optical field distribution, a thick photo-absorbing layer or dissipation layer is always needed, which is feasible only with a few organic semiconductor materials and often brings processing difficulties.

By employing microcavities, the OPDs' response wavelength can be easily tuned in visible spectrum (400–700 nm)[81] based on above-gap absorption and in NIR wavelength range (810–1665 nm)[198] based on CT state absorption. However, by introducing microcavities, the photoresponse enhancement and selectivity are directly correlated to the optical interference, which is a double-edged sword, leading to the following drawbacks:

- The angular dependence of the photoresponse is an intrinsic property of cavity-based devices. Siegmund *et al.*[27] and Wang *et al.*[82] described this phenomenon and a 50 nm blue-shift of the resonance peak wavelength was observed with light incidence angles larger than ±45°. Within ±20°, the resonance did not shift more than 10 nm for a CT-OPD with the FWHM of 36 nm.[27] For application, the light acceptance cone can be reduced (*e.g.* ±15°) to ensure the spectroscopic accuracy of the measured signal.[82]
- Control of higher order cavity resonances. As expressed in eqn (5), to achieve the tunability of response wavelength (λ_m),

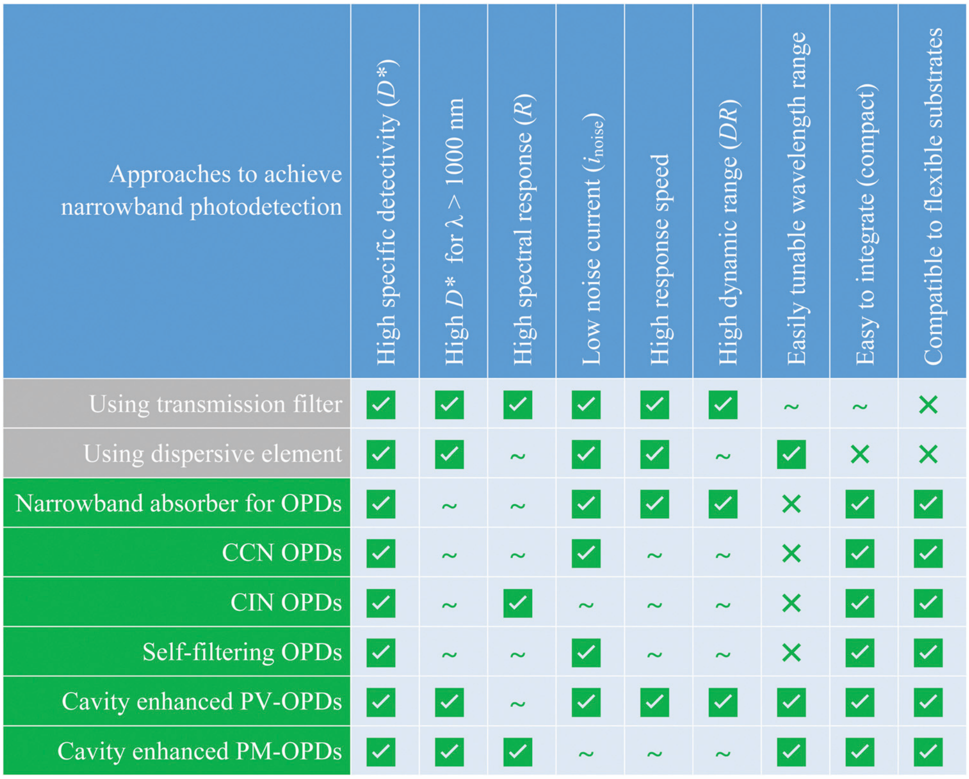

Approaches to achieve narrowband photodetection	High specific detectivity (D^*)	High D^* for $\lambda > 1000$ nm	High spectral response (R)	Low noise current (i_{noise})	High response speed	High dynamic range (DR)	Easily tunable wavelength range	Easy to integrate (compact)	Compatible to flexible substrates
Using transmission filter	✓	✓	✓	✓	✓	✓	~	~	✗
Using dispersive element	✓	✓	~	✓	✓	~	✓	✗	✗
Narrowband absorber for OPDs	✓	~	~	✓	✓	✓	✗	✓	✓
CCN OPDs	✓	~	~	✓	~	~	✗	✓	✓
CIN OPDs	✓	~	✓	~	~	~	✗	✓	✓
Self-filtering OPDs	✓	~	~	✓	~	~	✗	✓	✓
Cavity enhanced PV-OPDs	✓	✓	~	✓	✓	✓	✓	✓	✓
Cavity enhanced PM-OPDs	✓	✓	✓	~	~	~	✓	✓	✓

Fig. 14 Comprehensive summary of advantages and disadvantages of all different approaches to achieve narrowband photodetection in this review. In grey, the traditional approaches using filter or dispersive elements are shown. In green approaches based on OPDs are highlighted. The checkmark, tilde, and cross indicate whether a specific approach can either succeed, maybe succeed, or falls short in a certain category, respectively.

the microcavity thickness (L) needs to be varied, which can be realized by controlling the thickness of either transporting layer (ETL or HTL) or photo-absorbing layer in an OPD. A longer response wavelength requires a thicker cavity device. To realizing a wavelength tunability in range of 650–910 nm for second order resonance ($m = 2$), Tang *et al.* varied the photo-absorbing layer from 290 to 440 nm.[74] Higher order resonances usually lead higher EQE*s* and narrower FWHM but thicker cavities are required, which in turn brings the issue of depositing thick organic layers.

- Signal from other absorption regions. To avoid unexpected response signals induced by higher order resonances at shorter wavelengths than the design-resonance or the intrinsic main absorption of involved photo-absorbing materials, a bandpass filter or a layer of intrinsic photo-absorbing material might need to be integrated in front of the OPDs, increasing the processing complexity.[27]
- Photo-absorbing material combination for multiple wavelength sensing. As shown in Fig. 12b, stacked, multi-wavelength sensing OPDs are suffering undesired resonance cross-talk due to coherent coupling of both sub-cavities. The phenomenon can be suppressed by careful selection of the photo-absorbing material system combination. The materials are supposed to have large difference of absorption coefficient in the targeted wavelength range. Transfer matrix modelling can assist the selection by simulating the optical field distribution within both microcavities.

In Fig. 14, the advantages and disadvantages of the presented approach to achieve narrowband photodetection in OPDs are summarized and are compared to the traditional approaches of applying inorganic broadband PDs in conjunction with either optical transmission filters or dispersive elements.

State-of-the-art performance of recent narrowband OPDs

Fig. 15 visualizes the recent performance status of OPDs based on D^*, the most important performance metric of PDs, classified by fabricating methods (solution or vacuum processing) and spectral sensing bandwidth (broadband or narrowband). More information on the OPDs shown in Fig. 15 are summarized in Table 2, giving a detailed overview of the recent progress of state-of-the-art OPDs.

Potential applications of narrowband OPDs

Flexible and semi-transparent devices

Unlike their inorganic counterparts, organic semiconductors are mechanically soft and flexible and are deposited at low temperatures, allowing for their integration with flexible substrates such as polyimide (PI), polyethyleneterphthalate (PET), and poly(ethylene naphthalate) (PEN).[137] Krebs *et al.* demonstrated the first wearable OPDs based on the traditional

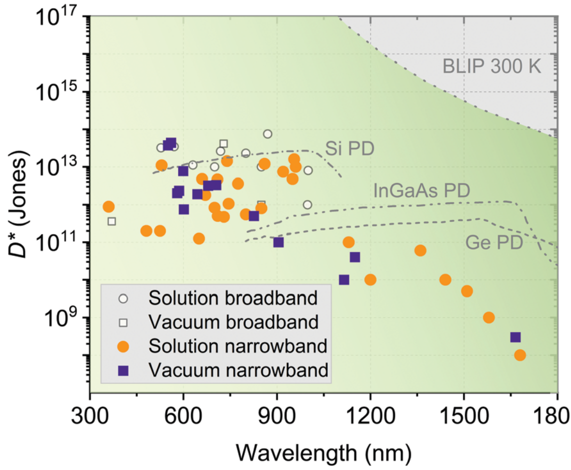

Fig. 15 *D** as a function of wavelength based on different device processing methods (solution *vs.* vacuum processing) and photodetecting wavelength bandwidths (broadband *vs.* narrowband detection). Further details about the individual devices are given in Table 2. The *D** of Si, InGaAs and germanium (Ge) are extracted from ref. 138. The BLIP limit is calculated at 300 K for photovoltaic PDs with a field-of-view of 2π.

architecture of PET/PEDOT:PSS/MEH-PPV:$PC_{61}BM$/Al.[215] Later, Eckstein *et al.* presented fully aerosol-printed flexible semitransparent OPDs on a PET substrate (Fig. 16a).[216] The flexible OPDs showed an equivalent performance to state-of-the-art devices fabricated on rigid substrates by conventional deposition methods. Subsequently, PI substrates flourished due to their durability in high-temperature processing. Zhong *et al.* first fabricated PI-based flexible OPDs with ultrashort channel length showing excellent responsivity and flexibility due to their unique structure design, as shown in Fig. 16b.[217]

Photoplethysmography (PPG) sensors

Healthcare plays a crucial role in our daily life and creates an ever-increasing demand for innovations in sensors. PPG, a non-invasive optical measurement technique, stands out in this field to accurately monitor health indicators such as pulse oximetry, heartbeat rate, and blood pressure. The PPG sensor typically comprises a light-emitting diode (LED) to illuminate the subcutaneous tissue and a PD to monitor light intensity variations related to changes in the blood volume in arteries. To penetrate deeper into the skin, and pick up signals from larger arterioles, red or NIR light with low attenuation is considered more suitable.[218] Huang *et al.* reported a highly sensitive NIR OPD based on a narrow-bandgap non-fullerene acceptor, CO1–4Cl, which showed a significant responsivity of 0.5 A W^{-1} in the spectral region from 920 to 960 nm.[219] As a preliminary assessment of the practical application of NIR OPDs, the authors carried out a PPG measurement (Fig. 17a). The light emitted from the LEDs is partially absorbed, reflected, and/or scattered by human tissue, which can be detected by an optical sensor with the changes in blood volume upon each cardiac cycle. These changes could be converted into electrical signals and were further analyzed to evaluate the heartbeat rate. From the typical systolic and diastolic peaks in a PPG profile, the author's heartbeat rate was determined to be 67 and 106 beats min^{-1} at resting and after-exercise conditions, respectively. Later, Fuentes-Hernandez *et al.* demonstrated a low noise OPD based on P3HT:ICBA BHJ with superior performance, rivaling low-noise silicon photodiodes (Si-PD) in all metrics within the visible spectral range, except response time (still video-rate compatible).[8] To exemplify the design opportunities of OPDs, a ring-shaped, large-area flexible PPG array was fabricated (Fig. 17b). The 1 cm^2 ring-shaped flexible OPD yielded PPG signals with a signal-to-noise ratio that is comparable to those measured with a 0.07 cm^2 Si-PD even when the electrical power of the red LED is reduced from 247 to 26 μW.

Pulse oximetry is another critical clinical application of PPG sensors for determining oxygen saturation in blood by optically quantifying the oxyhemoglobin (HbO_2) and deoxyhemoglobin (Hb) concentrations.[220] The first all-organic state-of-the-art pulse oximetry was reported by Lochner *et al.*[2] This sensor used green and red organic LEDs (OLEDs) and two spatially separated OPDs (Fig. 17c). The OPDs were based on the PTB7:$PC_{71}BM$ blend and exhibited a low leakage current of $\sim$1 nA cm^{-2} at -2 V with a -3 dB frequency above 10 kHz. This device measured oxygenation accurately with relative errors as small as 2%. These metrics were sufficient for oximetry measurements and notable because it was created on a flexible substrate, with the active layers of the sensor deposited by spin-coating and printing. Khan *et al.* reported a large-area, 2D reflectance oximeter array based on a flexible organic optoelectronic system, which comprised four red, four NIR OLEDs, and eight OPDs (Fig. 17d).[3] The OPD and OLED arrays were also fabricated by printing techniques. The implementation of the array provided 2D oxygenation mapping capability of an area rather than a single point, as demonstrated in previous related work.

In the aforementioned practical application, broadband OPDs and two spectrally distinct LEDs were employed to measure oxygen saturation. Attributing the OPD signal to one of the operated LEDs requires the modulation of the LED in the time domain and the correlated detection of the PD signals. Such a measurement setup needs elaborated measurement devices. Instead, employing two different narrowband OPDs would allow, on the one hand, to use a broadband light source and, on the other hand, to easily discriminate the spectral information since both wavelength ranges are measured separately. These advantages enable the use of a more straightforward measurement setup and increase the accuracy of the measurement analysis.

Image sensors

OPDs are increasingly investigated for imaging technologies, as their properties make them attractive candidates for applications such as VIS-color or NIR imaging, biometric imaging, fingerprint imaging, *etc.* OPDs offer cheaper processing methods, light, flexible, large (or small) areas and compatible device possibilities, and tunable optoelectronic properties – both at a material and device level. In 1998, Heeger *et al.* demonstrated the first full-color image sensors based on OPD arrays with

Table 2 Figures-of-merit and progress of recent state-of-the-art OPDs. The numbers highlighted in italics were not given in the original publication and are here calculated/estimated based on other correlated data provided in the respective publication. NBM, SF and MC are abbreviations for narrow bandgap materials, self-filtering and microcavity, respectively

Photo-absorbing materials	Type	Target peak [nm]	Spectral range [nm]	FWHM [nm]	D^* [Jones]	EQE [%]	R [A W^{-1}]	Bias [V]	LDR [dB]	$f_{-3\mathrm{dB}}$ [kHz]	Year	Ref.
Solution broadband												
PCDTBT:PC$_{61}$BM		528	300–800		$3.2 \times 10^{13\,a}$	27.00	0.31	−2.0	148	91.0	2016	146
PCDTBT:PC$_{71}$BM		570	400–720		3.5×10^{13}	76.00	*0.35*	−5.0	100	50.0	2015	202
PCDTBT:PC$_{71}$BM		532	300–800		$\sim 1.0 \times 10^{13\,b}$	70.00	*0.30*	−1.0	180	1000.0^{c}	2014	203
PBDB-T:PbS-TBAI		630	400–1000		1.1×10^{13}	*334.60*	1.70	−40.0	65	—	2018	204
PBDTTT-C:PC$_{71}$BD		700	350–800		$\sim 1.0 \times 10^{13}$	30.00	*0.17*	−2.0	~140	~20.0	2013	205
NT40:N2200		720	300–850		2.6×10^{13}	56.00	0.33	−0.1	97	~10.0	2019	206
PDDTT:PC$_{61}$BM		800	300–1450		$2.3 \times 10^{13\,d}$	25.00	*0.16*	−0.5	~100	—	2009	16
PDPP3T:PC$_{71}$BM		850	300–1000		$\sim 1.0 \times 10^{13}$	28.00	0.19	−0.5	148	400.0^{e}	2015	207
CS-DP:PC$_{71}$BM		850	300–1000		$8.0 \times 10^{12\,f}$	48.00	0.33	0	—	—	2018	208
NT40:IEICO-4F		870	300–1000		7.5×10^{13}	57.20	0.40	−0.1	123	~100	2021	209
Vacuum broadband												
C$_{60}$		370	300–700		3.6×10^{11}	~40.00	0.12	−6.0	*180*	95.0	2013	210
ClAlPc: C$_{70}$		730	300–800		$4.1 \times 10^{13\,g}$	74.60	0.44	−2.0	173	778.7	2020	211
Cy7-T:C$_{60}$^{h}		850	600–870		1.0×10^{12}	23.00	0.17	−2.0	*~100*	—	2015	22
Solution narrowband												
1(Pyrl):C$_{60}$	NBM	481	420–550	76	2.0×10^{11}	18.00	0.07	0	—	—	2019	177
PCDTBT:PC$_{71}$BM	CCN	670	610–800	85	1.8×10^{12}	35.00	0.10	−1.0	160	95.0	2015	24
DPP-DTT:PC$_{71}$BM	CCN	950	900–1020	80	4.8×10^{12}	*7.31*	0.06	−1.0	—	—	2015	24
P3HT:PC$_{61}$BM:CdTe	CCN	660	650–850	100	4.8×10^{12}	200.00	*1.06*	−6.0	220	900.0	2016	212
P3HT:PC$_{71}$BM	CIN	650	640–700	28	$1.4 \times 10^{11\,i}$	53500.00	278.00	−60.0	160	—	2017	25
P3HT:PC$_{71}$BM	CIN	800	790–800	30	$5.5 \times 10^{11\,j}$	2000.00	0.85^{k}	−50.0	170	—	2018	193
P3HT:PTB7-Th:BEH	CIN	850	830–880	27	8.0×10^{11}	15300.00	105.00^{l}	−13.0	145	—	2021	213
F8T2:ZnO	PM	360	350–400	20	8.8×10^{11}	2170.00	6.5	−15.0	—	0.1	2018	214
PTB7:PC$_{71}$BM	SF	745	645–745	50	1.1×10^{12}	*4.51*	0.03	0	103	38.5	2020	83
NT812:Y6	SF	860	860–960	50	1.2×10^{13}	61.00	0.42	−0.1	—	—	2020	26
DT-PDPP2T-TT:Y6	SF	920	860–960	40	7.4×10^{12}	—	—	−0.1	—	—	2020	26
DT-PDPP2T-TT:Y6	SF	955	860–960	50	1.6×10^{13}	—	—	−0.1	—	—	2020	26
PBDB-T:m-ITIC	SF	700	750–950	120	8.3×10^{11}	*53.00*	0.30	0	—	80.0	2020	73
PBTTT:PC$_{61}$BM	MC	775	700–1100	15	3.6×10^{12}	40.00	*0.25*	0	130	—	2017	74
PBTTT:PC$_{61}$BM	MC	960	700–1100	17	1.0×10^{13}	24.00	*0.19*	0	130	—	2017	74
PDPPTDTPT:SdiCNPBI	MC	1200	1000–1700	35	1.0×10^{10}	0.90	*0.01*	0	—	—	2017	74
PDPPTDTPT:SdiCNPBI	MC	1440	1000–1700	38	1.0×10^{10}	0.10	*1.16×10^{-3}*	0	—	—	2017	74
PDPPTDTPT:SdiCNPBI	MC	1580	1000–1700	47	1.0×10^{9}	0.05	*6.37×10^{-4}*	0	—	—	2017	74
PDPPTDTPT:SdiCNPBI	MC	1680	1000–1700	41	1.0×10^{8}	0.01	*1.36×10^{-4}*	0	—	—	2017	74
PCDTPTSe:PC$_{71}$BM	MC	710	650–1510	60	$\sim 5.0 \times 10^{11}$	18.00	*0.10*	0	146	—	2021	18
PCDTPTSe:PC$_{71}$BM	MC	1130	650–1510	45	$\sim 1.0 \times 10^{11}$	6	*0.05*	0	—	—	2021	18
PCDTPTSe:PC$_{71}$BM	MC	1360	650–1510	35	$\sim 6.0 \times 10^{10}$	1.9	*0.02*	0	—	—	2021	18
PCDTPTSe:PC$_{71}$BM	MC	1510	650–1510	20	$\sim 5.0 \times 10^{9}$	0.15	*1.83×10^{-3}*	0	—	—	2021	18
Vacuum narrowband												
ZnPc:C$_{60}$	MC	905	875–1085	43	1.0×10^{11}	22.00	*0.16*	0	*~100*		2017	27
TPDP:C$_{60}$	MC	—	810–1550	—	—	—	—	0	—	—	2017	27
DCV5T-Me:C$_{60}$	MC	645	400–700	84	1.9×10^{12}	50.00	0.27	0	130	5000.0	2019	81
D8:C$_{60}$	MC	1150	810–1150	50	4.0×10^{10}	0.25	*2.32×10^{-3}*	0	—	—	2019	197
D8:C$_{60}$	MC	1665	810–1665	50	3.0×10^{8}	4.50×10^{-3}	*6.04×10^{-4}*	0	—	—	2019	197
ZnPc:C$_{60}$	MC	877	790–1180	37	1.0×10^{11}	10.00	*0.071*	0	120	—	2020	82
D6:C$_{60}$	MC	1115	1020–1435	58	1.0×10^{10}	0.15	*1.40×10^{-3}*	0	139	—	2020	82
ZnPc:C6$_{0}$	MC	826	826–879	17	5.0×10^{11}	75	*0.50*	−10	—	19.44^{m}	2021	201

[a] D^* calculated at wavelength 566 nm. [b] D^* calculated at bias voltage of −0.5 V. [c] The $f_{-3\mathrm{dB}}$ measured at bias voltage of −5.0 V. [d] D^* calculated at bias voltage of −0.5 V. [e] The $f_{-3\mathrm{dB}}$ characterized at bias voltage of −1.0 V. [f] D^* calculated at wavelength 1000 nm. [g] D^* calculated without bias. [h] The Cy7-T and C$_{60}$ were spin-coated and evaporated, respectively. [i] D^* measured at −10 V bias. [j] D^* measured at −10 V bias. [k] R measured at −10 V bias. [l] Incorrectly calculated by the authors. [m] The measured device had peak wavelength at 843 nm.

P3OT:PC$_{61}$BM polymer blend.[221] After that, Rauch *et al.* extended the detection region up to 1.8 μm and realized an outstanding NIR image sensor based on PbS quantum dots (QDs) sensitized OPDs (Fig. 18a).[170] For a 4 mm^2 diode, accelerated aging test results showed minimum lifetimes of at least one year. Moreover, the NIR OPDs were integrated on top of commercially available a-Si active-matrix thin-film transistor (TFT) panels with 256 × 256 pixels and a photo of a butterfly was successfully reconstructed under an infrared illumination wavelength of 1310 nm. This work first demonstrated NIR imaging with hybrid photodetectors (HPD). Later, Büchele *et al.* designed another HPD for X-ray imaging by incorporating terbium-doped gadolinium oxysulfide scintillator (GOS:Tb) particles into a P3HT:PC$_{61}$BM blend on an a-Si:H

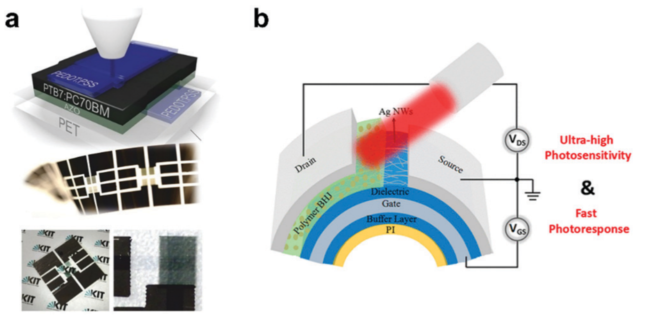

Fig. 16 (a) Schematic structure and photographs of fully-printed ITO-free OPDs on PET foil showing their semi-transparency and mechanical flexibility.[216] (b) Device structure of flexible PT-OPDs with ultrashort channel length.[217] (a) Reproduced with permission.[216] Copyright 2015, WILEY-VCH GmbH. (b) Reproduced with permission.[217] Copyright 2018, American Chemical Society.

TFT array backplane with ITO contact pads (Fig. 18b).[222] The X-ray-induced light emission from the scintillators is absorbed within hundreds of nanometers, which is negligible compared with the pixel size. Hence, the optical crosstalk is minimized. The X-ray image sensors exhibit an excellent spatial resolution of 4.75 linepairs per mm (lp mm^{-1}) at a modulation transfer function of 0.2. Xu *et al.* reported 10,000-pixel OPDs focal plane arrays (FPAs) on the top of a 1.0 cm radius plastic hemisphere to imitate the structure of the human eye (Fig. 18c).[223] The CuPc/C_{60} active layer was evaporated across the entire surface of the hemisphere, followed by deposition of a thin Ag strike layer and an array of Ag cathode columns on top. The impulse response of the OPDs is as fast as 20 ± 2 ns and measured a dynamic range of 20 dB, which makes the FPAs suitable for video-recording applications. Recently, Yokota *et al.* realized a flexible image sensor that integrated polycrystalline Si TFT readout circuits and NIR OPDs, capturing images of veins and fingerprints (Fig. 18d).[224] Narrowband polymer PMDPP3T blended with $PC_{61}BM$ was used as the active layer, enabling a NIR OPD that exhibited a high sensitivity of 0.57 A W^{-1} when driven at −2 V at a NIR wavelength of 850 nm as is commonly done for vein authentication. This is equivalent to the

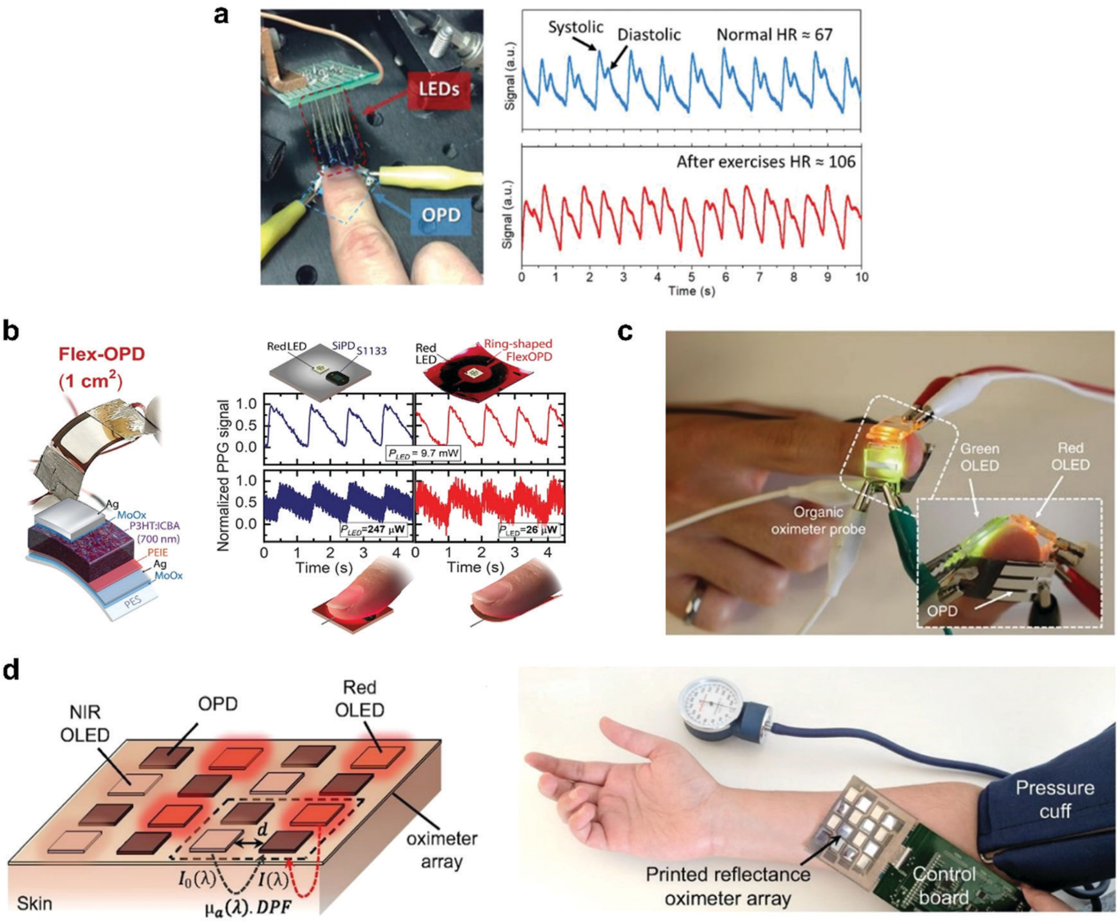

Fig. 17 (a) Setup measuring the heart rate using OPDs and the recorded pulse signals.[219] (b) Flexible OPD device geometry, schematics of S1133 Si-PD and ring-shaped flexible OPD PPG array (top) and comparison of reflection-mode PPG signals measured on a finger with both PDs driven by a red LED operated at different electrical power values.[8] (c) Photograph of the OLED-OPD configuration for an all-organic pulse oximeter.[2] (d) The schematic configuration and photograph of the reflectance oximeter array.[3] (a) Reproduced with permission.[219] Copyright 2019, WILEY-VCH GmbH. (b) Reproduced with permission.[8] Copyright 2020. The American Association for the Advancement of Science. (c) Reproduced with permission.[2] Copyright 2014, Springer Nature. (d) Reproduced with permission.[3] Copyright 2018, the Authors. Published by PNAS.

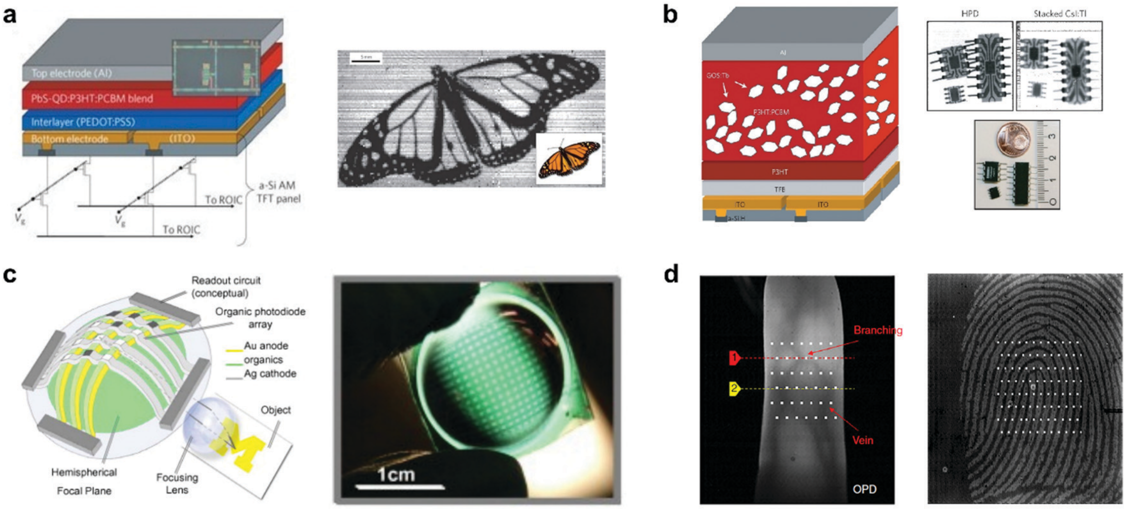

Fig. 18 (a) Schematic of the NIR image sensor array based on OPDs doped with QDs and infrared shadow cast by a monarch butterfly.[170] (b) Schematic of the X-ray image sensor with a high resolution based on organic BHJ doped with GOS:Tb.[222] (c) Schematic and photograph of the hemispherical OPD-based FPA that imitates the human eye.[223] (d) The image of veins and fingerprints through the flexible image sensor.[224] (a) Reproduced with permission.[170] Copyright 2009, Springer Nature. (b) Reproduced with permission.[222] Copyright 2015, Springer Nature. (c) Reproduced with permission.[223] Copyright 2008, Elsevier B.V. (d) Reproduced with permission.[224] Copyright 2020, Springer Nature.

sensitivity of Si photodiodes (0.5–0.7 A W^{-1}). The conformable imager, with a resolution of 508 pixels per inch, a speed of 41 frames per second, and a total thickness of only 15 μm, can be further proven by the veins' clear image in the finger fingerprint.

Spectrometers

In 2017, Tang *et al.* employed a resonance optical cavity device architecture to fabricate a tunable wavelength-selection OPD exploiting weak sub-gap absorption of intermolecular CT states.[74] This concept enables highly wavelength selective NIR OPDs with remarkable D^* comparable with commercial inorganic counterparts. Based on this approach, a prototype miniaturized spectrometer was demonstrated by using a blade-coated active layer with gradient thickness (Fig. 19a). The transmittance spectrum of water was successfully measured, indicating a sufficient spectral resolution for a potential application in moisture detection. Recently, Yang *et al.* also utilized the cavity concept to build narrowband OPDs based on the PCDTPTSe:$PC_{71}BM$ active layer combined with a thick ZnO

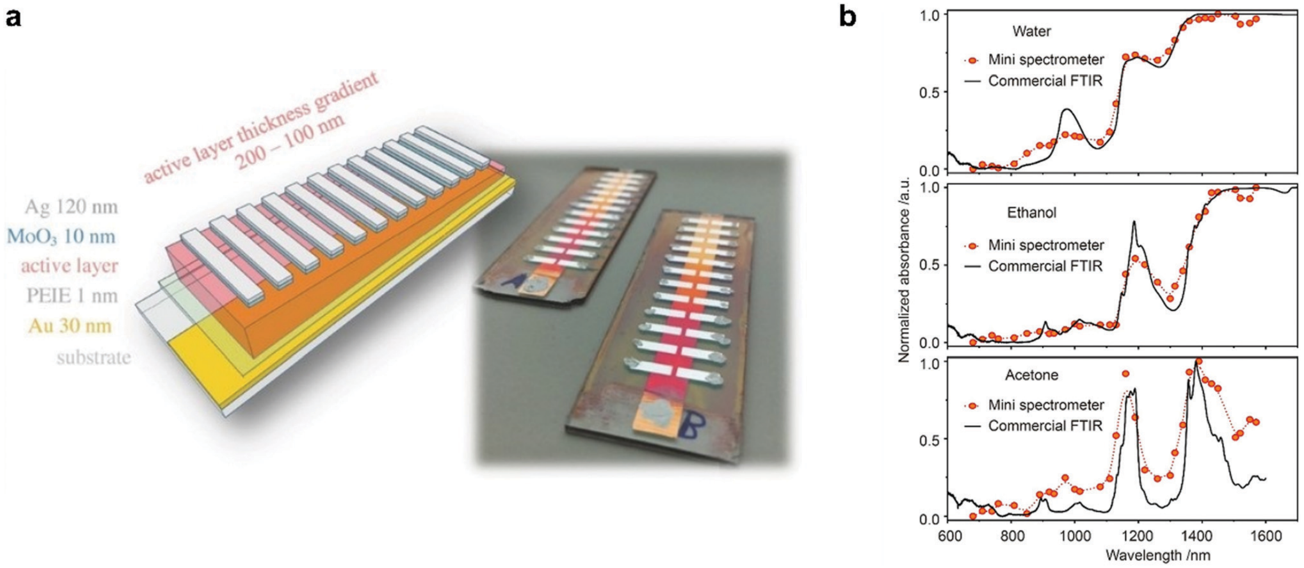

Fig. 19 (a) A schematic and a photograph of a miniaturized spectrometer based on cavity enhanced NIR OPDs.[74] (b) Absorption spectra of water, ethanol, and acetone measured using the miniaturized spectrometer compared to the spectra measured with a commercial Fourier transform infrared spectrometer.[18] (a) Reproduced with permission.[74] Copyright 2017, WILEY-VCH GmbH. (b) Reproduced with permission.[18] Copyright 2021, American Chemical Society.

spacer.[18] Similarly, a series of OPDs with varying response wavelengths in the range of 660–1600 nm was selected to prove the potential in spectroscopic applications. Using a halogen lamp as an external light source, the characteristic absorption features of water, ethanol, and acetone were well resolved, as shown in Fig. 19b.

Miniaturized spectrometers are very attractive for mobile applications of spectroscopy to create new applications and products. In the NIR wavelength range, many characteristic absorption features of organic compounds are manifested and their analysis allows for qualitative and quantitative investigation of solids (reflection mode) and liquids (transmission or trans-reflection mode). Potential applications are the differentiation of materials such as fabrics (*e.g.*, silk, wool, polyester, nylon), plastics (*e.g.*, PET, PE, PVC, PP, PS), or many others. Such identification allows for a broad application in consumer and industry products, especially for the automatization of certain processes and machines. Another aspect is that NIR absorption and reflection features can be utilized to authenticate substances. This is becoming an important segment since many companies want to prevent the replication of their products by other manufacturers. For this purpose, native NIR reflection features of the product or specially designed, non-visible control-features can be utilized. An additional application in this regard can be the immediate identification of harmful and not-wanted substances such as drugs in liquids.

Finally, NIR spectroscopy is a very powerful method for quantitatively measuring the composition of solids and liquids, which is useful for countless applications. Here, NIR spectroscopy allows for a non-invasive, quick and precise analysis and thereby provides information that is usually rather difficult to obtain. For example, the ethanol content of a beverage can be precisely measured which is important not only for the producer but also for tax accounting and customs when trading beverages. For many processes, the composition of compounds is essential to sustain a very high production quality. One example is the qualification of fruit ripeness directly in the field to obtain the highest quality goods. Another example is the determination of moisture, which plays an important role in many automated processes, *e.g.*, the production of corrugated cardboard. Applying spectroscopy allows for real-time, contactless measurement of water content in materials and is the prerequisite for further optimization of the production process. All in all, low-cost and highly integrated narrowband NIR-OPDs have a great potential to transform the well-established spectroscopy into the mobile application and bring the former laboratory know-how directly (or indirectly) to everyone. This transformation of an established technology has great potential for many innovative and smart products.

Conclusion and perspective

In this review, we summarized the status, recent progress and current challenges of narrowband OPDs. They have drawn much attention in the past decade thanks to advanced properties such as lightweight, flexibility, low-cost, large-area scalability, bio-compatibility and semi-transparency. These properties make narrowband OPDs potentially meet the demand of nowadays smarter and more efficient digital life. To date, the performance of state-of-the-art OPDs is dramatically improved, benefitting from the rapid progress in design and synthesis of new organic semiconductor compounds. In principle, narrowband OPDs rely on narrow-photo-absorbing materials covering the detection spectrum from the visible to the NIR range.[20–22,72] However, such narrowband OPDs based on narrow-photo-absorbing materials with a specific bandgap are still suffering from a lack of material candidates, and also each material can only supply one specific spectral detection window. Fortunately, this issue was solved by the emerging strategies based on device architecture engineering, utilizing the usual organic broadband absorber. In 2015, charge collection narrowing OPDs were first introduced by using broadband-absorbing materials and a thick junction strategy, achieving red and NIR OPDs with FWHM of less than 100 nm.[24] Afterwards, self-filtering narrowband OPDs composed of a depletion layer, a donor and a thin acceptor layer, forming a planar heterojunction, were demonstrated.[26,83] In 2017, narrowband OPDs with the combination of a Fabry–Pérot microcavity and the charge-transfer state absorption of a bulk heterojunction were realized.[27] Later on, based on such strategies, narrowband OPDs fabricated by either solution processing[18,74] or vacuum thermal evaporation[81,82,197,198] were explored extensively. The tunability of narrowband OPDs was radically improved, with the spectral detection window covering the visible (400–700 nm)[81] and NIR (810–1665 nm) range.[197] As application demonstrations, transmission spectra of different liquids (water, ethanol, acetone) were determined by spectrometers composed of narrowband OPDs.[18,74] Having made this great progress, narrowband OPDs are already on the way to being commercialized for application-specific tasks (Fig. 20a), in particular for mobile usage of spectroscopy (Fig. 20b). Here, the key advantages of organic semiconductors such as simple and low-cost

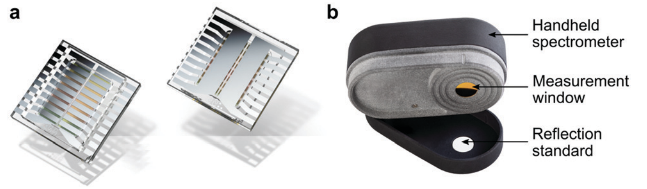

Fig. 20 (a) Miniaturized spectrometer OPD-chip in top (left side) and bottom view (right side), being commercialized by the Senorics GmbH (Dresden, Germany, https://senorics.com/). The spectrometer chip is composed of 16 independent narrowband NIR-OPDs with an overall area of 121 mm^2 (11 mm × 11 mm). The OPD-chip is bottom illuminated and its upper side is encapsulated by a glass lid to prevent ambient influences. (b) A handheld spectrometer employing the NIR OPD-chip from figure (a) and a NIR light source, realized by the same company. During measurement, NIR light shines through the measurement window onto the target object, which is exposed in front of the window and the reflected light is analyzed by the chip. The lid of the handheld spectrometer has an integrated reflection standard which is used to perform a white reference measurement. Reproduced with permission. Copyright, Senorics GmbH.

production, broad tunability of electrical and optical properties as well as competitive performance are the essential properties making this technology very promising. Nevertheless, there are still several important research perspectives for organic-semiconductor-based photodetectors:

- Obviously, there will be always a need for better materials, with properties like high absorption coefficient, broad- or narrowband absorption depending on device principle, and excellent charge carrier generation. In particular, there is a need for stronger absorbers in the NIR up to 2000 nm since many applications require signal detection in this spectral range. Besides the optical properties mentioned above, these materials also need to have good processability, low synthesis cost and good photostability.
- There is a need for novel device principles, which allow to realize specific properties, such as high detectivity, narrowband operation, and high speeds or a combination thereof. For instance, there are many principles which have not yet been intensively investigated, such as two- or three-dimensional patterning of structures.
- For devices working in photovoltaic mode, understanding and controlling reverse current is still a key issue. The rather complicated nanostructured bulk heterojunctions employed in most of these devices make it difficult to understand traps in particular at the interfaces. It is essential to understand the intrinsic limits in terms of reverse current and avoid extrinsic currents.
- The field of OPDs with gain is still not well understood. Many of the devices show quite good device parameters, without microscopic understanding of the device principle. Only such an understanding will allow for a directed optimization.
- To fully harvest the intrinsic advantages of organic electronics, the integration of OPDs with organic transistors is of great interest. This could provide immediate amplification of the detector signal, or even a certain *in situ* pre-processing leading towards more autonomous organic sensor modules.
- It would be highly desirable to develop organic detectors with speeds in the GHz range and beyond. Recently, first GHz organic pin-diodes have been shown[160] and it remains a challenge to prove such operation speeds for optical detection.
- Finally, the temporal stability of OPDs has been much less investigated than their organic counterparts (*i.e.* organic light emitting diodes and organic solar cells). There is hope that OPDs are very stable since their relatives, the organic solar cells, achieve encouraging operational stabilities.[85,225]

We are convinced that these exciting perspectives will stimulate further research on OPDs. As the success of organic light emitting diode displays has shown that the materials and deposition methods are ready for mass-scale manufacturing. In a sensor-hungry world, OPDs will thus have a bright future!

Conflicts of interest

Karl Leo is shareholder of Senorics GmbH, a company active in organic photodetectors.

Appendix – performance metrics of organic photodetectors

A fair comparison of different PD technologies and a valid evaluation of photodetecting devices requires a careful determination of fundamental performance metrics. Here, we summarize the performance metrics of PDs. In the formulas below the corresponding units are indicated in parenthesis.

Quantum efficiency

The quantum efficiency of a photodiode indicates the amount of photogenerated charge carriers produced by the PD when illuminating it with photons of a specific wavelength. By integrating the quantum efficiency over the electromagnetic spectrum of the light source, the total current produced by the PD can be evaluated. There are two types of quantum efficiencies utilized to characterize PDs:

- The external quantum efficiency (EQE) is given by the ratio of the number of charge carriers extracted at the electrodes of a PD to the total number of incident photons impinging onto the device:

$$\mathrm{EQE}(\lambda) = \frac{\#\,\text{extracted charge carriers}}{\#\,\text{photons}} = \frac{I_{\mathrm{ph}}/q}{P_{\mathrm{ph}}/h\nu} \quad (1\ \text{or}\ \%), \qquad (6)$$

where I_{ph} is the photogenerated current, q the elementary charge, P_{ph} the incident light power, h the Planck constant, and ν the frequency of the photons.

- In contrast to the EQE, the internal quantum efficiency (IQE) refers only to photons that are absorbed by the active layer. Thus, it refers to the ratio of the total number of charge carriers extracted from the device to the number of incident photons that are absorbed in the photo-active layer. The IQE of a PD yields the overall efficiency of the charge carrier generation, dissociation, recombination and extraction processes *versus* the wavelength or energy of incident photons.[87] Often, IQE is calculated from the EQE by measuring the transmission ($\mathcal{T}$) and reflection ($\mathcal{R}$) of a PD as expressed in eqn (7). This approach neglects parasitic absorption and the interference of an optical cavity, which is introduced by the mirror-like electrodes. Armin *et al.* carefully treated this issue and gave a more precise solution to calculate the IQE as formulated in eqn (8).[87] The metallic electrode is assumed to be opaque, hence, $\mathcal{T}$ is not accounted for in eqn (8). The parasitic absorption ($A_{\mathrm{parasitic}}$) and the optical field distribution of photodiodes can be determined by transfer matrix simulations.[87]

$$\mathrm{IQE} = \frac{\mathrm{EQE}}{1 - \mathcal{R} - \mathcal{T}} \quad (1\ \text{or}\ \%). \qquad (7)$$

$$\mathrm{IQE} = \frac{\mathrm{EQE}}{1 - \mathcal{R} - A_{\mathrm{parasitic}}} \quad (1\ \text{or}\ \%). \qquad (8)$$

Responsivity

The responsivity (R), also referred to as spectral response, is defined as the ratio of the generated photocurrent (I_{ph}) to the incident light power (P_{ph}) at a corresponding wavelength. In practice, R is often calculated from EQE.

$$R = \frac{I_{\mathrm{ph}}}{P_{\mathrm{ph}}} = \mathrm{EQE} \cdot \frac{q\lambda}{hc} \approx \mathrm{EQE} \cdot \frac{\lambda(\mathrm{nm})}{1239.8} \quad (\mathrm{A\ W^{-1}}), \tag{9}$$

where λ is the wavelength expressed in nm.

Noise current (I_{noise}) and noise equivalent power (NEP)

In a real measurements, the final criterion to detect a weak signal is the ratio of signal to noise. It is therefore very important to understand the sources of noise in PDs. Inclusion of noise leads from the responsivity to the detectivity which is discussed below.

There are several sources contributing to the device noise and the current associated to it, I_{noise}. The white noise components (frequency independent) entail the thermal noise (I_{thermal}), also called Johnson-Nyquist noise, the shot noise (I_{shot}) and the generation-recombination noise ($I_{\mathrm{G-R}}$). Additionally, pink noise components (frequency dependent) are also observed. The most known but least understood pink noise is the flicker or simply "one over f" noise ($I_{1/f}$ noise), which is commonly observed in the low frequency regime of the spectral noise density. Together, these noise components determine the detection limit for low intensity light.[138,226]

- I_{thermal} exists in any resistive component and is generated by the random thermal motion of charge carriers. In OPDs, it can be correlated with the total parallel resistance (R_{p}) including shunt resistance (R_{shunt}) and effective diode resistance at zero bias in the circuit. In most conditions, R_{shunt} dominates the R_{p}.[138] Therefore, I_{thermal} can be formulated into:

$$\left\langle {I_{\mathrm{thermal}}}^2 \right\rangle = \frac{4k_{\mathrm{B}}T}{R_{\mathrm{shunt}}}\Delta f \quad (\mathrm{A}^2), \tag{10}$$

where k_{B} is the Boltzmann constant, T the absolute temperature, and Δf the measurement bandwidth, which defines the frequency range in which the noise is recorded. Ideally, Δf is a perfectly rectangular bandpass filter with a bandwidth of 1 Hz. Practically, such a circuit is not feasible and a measurement at these conditions would take infinite time. Therefore, an equivalent bandwidth is defined, which, for electrical measurements integrated over a time Δt, reads $(2\Delta t)^{-1}$.[227]

- I_{shot} arises from the discrete character of charge carriers when overcoming energy barriers. In p–n, p–i–n, or Schottky junctions, for example, the current suffers small time-dependent variations caused by charge carriers individually crossing depletion regions or the Schottky injection barrier. I_{shot} is therefore proportional to the average dark current I_{d} (without illumination):[136]

$$\langle {I_{\mathrm{shot}}}^2 \rangle = 2qI_{\mathrm{d}}\Delta f \quad (\mathrm{A}^2). \tag{11}$$

- $I_{\mathrm{G-R}}$ is the result of temporal variation of the background photon flux, which leads to a variation in the charge carrier concentration, thereby affecting the photoconductivity in photoconductors or the photocurrent in photodiodes. Although the G–R noise is white in nature, a pink behavior can be observed depending on the dynamics of the system. For band-to-band processes, for example, G–R noise becomes frequency dependent at the frequency corresponding to the reciprocal of the transit time.[228] Because G–R noise in photodiodes can be expressed with a mathematically equivalent expression to that of shot noise,[229] both noise sources are often thought to be the same, with the former attributed to photoconductors and the latter to photodiodes. The confusion arises from the fact that in photodiodes operated under reverse bias, only generation is relevant, since charges are swept out of the device and do not recombine.[228] In photoconductors, however, both processes take place randomly. Yet, strictly speaking, the physical nature of these two sources of noise is different. Finally, $I_{\mathrm{G-R}}$ is expressed by eqn (12), assuming the mathematical form of eqn (11) for photodiodes operating under reverse bias.[228,229]

$$\langle {I_{\mathrm{G-R}}}^2 \rangle = 4qI_{\mathrm{d}}\Delta f \quad (\mathrm{A}^2). \tag{12}$$

- $1/f$ noise: the spectral distribution of flicker noise can be empirically described by eqn (13), where K is a normalization constant, $a \approx 2$ and, $b \approx 1$.[227,230] While physical explanations have been given for the aforementioned sources of noise, $1/f$ noise remains mysterious, being reflected in the lack of a proper name. It is common to observe a frequency dependent increase of the noise at low frequencies, which follows a $1/f$ behavior. The most accepted explanation for the origin of this effect is related to surface traps and bulk traps, leading to a fluctuation in the charge carrier density, as charges fall into and are released from these states. However, none of these effects have been completely clarified.[227] In organic semiconductor devices, $1/f$ noise is introduced by resistance fluctuation and intrinsically caused by either charge carrier fluctuation or mobility fluctuation.[226,231]

$$\left\langle {I_{1/f}}^2 \right\rangle = \frac{KI^a}{f^b}\Delta f \quad (\mathrm{A}^2). \tag{13}$$

Generally, it is challenging to analyze all of the components contributing to I_{noise}. Hence, the I_{noise} for PDs is often estimated by considering the white noise (I_{shot} and I_{thermal}) and $I_{1/f}$ for low frequencies. Consequently, I_{noise} can be expressed by:

$$\left\langle {I_{\mathrm{noise}}}^2 \right\rangle = \left(2qI_{\mathrm{d}} + \frac{4k_{\mathrm{B}}T}{R_{\mathrm{shunt}}} + \frac{KI^a}{f^b}\right)\Delta f \quad (\mathrm{A}^2). \tag{14}$$

The noise equivalent power (NEP) denotes the sensitivity of OPDs, representing the lowest detectable light power, expressed in the unit W Hz$^{-1/2}$ and is defined as the power of the incident light at which the signal-to-noise ratio (SNR) is unity at 1 Hz output bandwidth. The SNR is the ratio of the photogenerated current to noise current (I_{noise}). A smaller NEP value indicates a higher sensitivity of PDs. The NEP can be determined by measuring the light intensity dependent photocurrent and can be written as:[158,226]

$$\mathrm{NEP} = \frac{I_{\mathrm{noise}}}{\sqrt{\Delta f}R} = \frac{S_{\mathrm{n}}}{R} \quad \left(\mathrm{W\ Hz^{-1/2}}\right). \tag{15}$$

where S_{n} is referred to as noise spectral density, describing the spectral (at every frequency) density of noise per unit of bandwidth, expressed in A $\text{Hz}^{-1/2}$ or in V $\text{Hz}^{-1/2}$, when measured in volts.

Specific detectivity (D^*)

Due to the counterintuitive character of the NEP, where a better PD has lower NEP, its inverse was introduced, named detectivity (D). Additionally, it is possible to show that D is inversely proportional$\sqrt{A}$, where A is device area in cm^2.[37,232] Therefore, in order to compare different PDs, D is normalized by $\sqrt{A}$, being referred to as specific detectivity (D^*).

$$D^* = \frac{\sqrt{A}}{\text{NEP}} = \frac{R\sqrt{\Delta f A}}{I_{\text{noise}}} \quad (\text{cm Hz}^{1/2}\ \text{W}^{-1} \text{ or Jones}). \qquad (16)$$

D^* of current OPDs mostly range from 10^{11} to 10^{13} Jones. Some recent research promotes values closer to 10^{13} Jones or even above by further reducing the dark current, a value that is comparable to D^* of commercial Si PDs.[8,16,26,146,203] It is noteworthy that D^* of either organic or inorganic PDs are still several orders of magnitude lower than the dark adapted human visual perception ($\sim 10^{17}$ Jones).[233]

Dynamic range (DR) and linear dynamic range (LDR)

Every PD operates in an optical input range where its photoresponse can be accurately measured and predicted. This range, from the lowest to the highest optical input which generates such a predictable photoresponse, is referred to as dynamic range (DR). Often, DR is taken from the region where the photoresponse is proportional to a power law of the optical input, *i.e.* $I \propto \text{Irr}^{\beta}$, where I and Irr are the photocurrent and irradiance, respectively. Such dependence corresponds to a linear behavior in the double-log plot. Photoconductors with photogain (G) higher than unity show a sublinear DR with $\beta < 1$,[34,234] while photodiodes often show a rather linear photoresponse referred to as linearity or linear dynamic range (LDR) with $\beta = 1$. Physically, LDR means that within this range, the processes of charge carrier generation and recombination are independent of the light intensity, which is translated to a linear dependence of the photoresponse on the latter. While a linearity is desired for applications due to the facilitated device calibration, a non-linear photoresponse can likewise be used, as long as the non-linearity is reproducible and, therefore, predictable. DR and LDR can be expressed respectively as:

$$\text{DR} = 20\log\left(\frac{\text{Irr}_{\max}}{\text{Irr}_{\min}}\right) \neq 20\log\left(\frac{I_{\max}}{I_{\min}}\right)\ (\text{dB}), \qquad (17)$$

$$\text{LDR} = 20\log\left(\frac{\text{Irr}_{\max}}{\text{Irr}_{\min}}\right) = 20\log\left(\frac{I_{\max}}{I_{\min}}\right)\ (\text{dB}), \qquad (18)$$

where $\text{Irr}_{\min}$ ($I_{\min}$) and $\text{Irr}_{\max}$ ($I_{\max}$) are the minimum and maximum detectable light intensity (photocurrent), respectively. Note that LDR requires a unity slope in the double-log plot ($\beta = 1$), which means that LDR can be extracted from the ratio of the maximum to the minimum irradiance or photocurrent. DR, on the other hand, must be extracted from the ratio of the maximum to the minimum irradiance. Up to now, the LDR of OPDs was extended up to 11 orders of magnitude, *i.e.* 220 dB, with suppressing the recombination losses.[24,27,79,235] It overwhelms the LDR of InGaAs ($\sim$132 dB)[16] and it is comparable with Si, GaP and GaAsP photodiodes, which can have LDR in the range of 220–240 dB.[16,146,203,236] In the literature,[16,65,210,212,237] sometimes 10·log is used, however, this definition usually applies for power quantities.[158]

Response speed

The response speed represents how fast PDs respond to the incident optical signal, which determines potential applications of PDs like imaging,[1,238] hemodynamics monitoring,[219] and high speed optical communications.[73,160] Response speed can be characterized by transient photocurrent measurements, where, by applying a short pulse of an optical signal, the rising (τ_r) and falling (τ_f) time of the PDs are revealed. τ_r is defined as the rising time of photocurrent from 10% to 90% of the maximum value when turning on the illumination. *Vice versa*, τ_f is defined as the time for the photocurrent to fall from 90% to 10% of the maximum value when turning off the illumination. The response speed is correlated to the charge carrier separation, dissociation, recombination, and extraction. For example, the conductivity of the electrodes influences the transit time of charge carriers;[239,240] an electron or hole blocking layer affects charge carrier extraction or injection.[63,241]

−3 dB bandwidth ($f_{-3\text{dB}}$)

Another important parameter for evaluating the response speed of PDs is the frequency response being quantified by the −3 dB bandwidth ($f_{-3\text{dB}}$). It is defined as the modulation frequency of the optical signal at which the measured photocurrent decreases to −3 dB ($1/\sqrt{2}$ = 70.7%) of its low frequency value. The $f_{-3\text{dB}}$ is correlated to the carrier transit time (τ_{tr}) and the RC-time of the equivalent circuit as:

$$(f_{-3\text{dB}})^2 = \left(\frac{3.5}{2\pi\tau_{\text{tr}}}\right)^2 + \left(\frac{1}{2\pi RC}\right)^2 \quad (\text{Hz}^2), \qquad (19)$$

where C is the capacitance of the device. R is the total series resistance composed by the series resistance of the measured device, contact resistance, sheet resistance and load resistance of the measurement circuit. Therefore, strategies such as reducing the device effective area and series resistance can be employed to improve $f_{-3\text{dB}}$.[73]

Spectral selectivity and spectral rejection ratio (SRR)

Additionally to the discussed figures-of-merit, there are two more parameters that need to be introduced for evaluating narrowband PDs. As depicted in Fig. 2, one is the full width at half maximum (FWHM), denoting the selectivity of PDs. The narrower the FWHM, the higher the selectivity. FWHM can either be defined from the EQE curve (FWHM_{EQE}) or the responsivity curve (FWHM_{R}). The other important parameter is the spectral rejection ratio (SRR), describing the ratio of the peak responsivity (R_{peak}) in the target spectral window to the responsivity outside this measurement window (R_{out}), expressed as:[73]

$$\mathrm{SRR} = \frac{R_{\mathrm{peak}}}{R_{\mathrm{out}}} \quad (1 \text{ or } \%). \tag{20}$$

In Fig. 2 (panel: spectral bandwidth), the SRR_1 (= $R_{\mathrm{peak}}/R_{\mathrm{out1}}$) is larger than SRR_2 (= $R_{\mathrm{peak}}/R_{\mathrm{out2}}$). Assuming a white light source impinging onto a PD, a larger SRR indicates that less signal originates from unwanted spectral regions. In real applications of narrowband PDs, a high SRR is needed to ensure a high signal specificity, *i.e.*, a signal that mainly corresponds to the targeted wavelength and only contains the smallest possible part of other wavelength ranges.

Abbreviations

PD	Photodetector
OPD	Organic PD
PC-OPD	Photoconductor OPD
PM-OPD	Photomultiplication OPD
PT-OPD	Phototransistor OPD
CT-OPD	Cavity-enhanced charge-transfer (CT) state based OPD
PV-OPD	Photovoltaic OPD
OSC	Organic solar cell
VIS	Visible
NIR	Near infrared
R	Spectral photoresponse
EQE	External quantum efficiency
D^*	Specific detectivity
FWHM	Full width at half maximum
SRR	Spectral rejection ratio
J_{D}	Reverse dark current
J_0	Saturation current

Acknowledgements

We acknowledge Jakob Wolansky and Louis Conrad Winkler for fruitful discussions and feedback to our manuscript. We further acknowledge the Senorics GmbH for their permission to include pictures of their miniaturized OPD-chip and spectrometer technology. Additionally, we thank the BMBF for funding through the projects "Pergamon" (16ME0012) and "Flexmonirs" (01DR20008A) and the German Research Foundation (DFG) through project "Coherent Perfect Light for Organic Microdevices" (442597684). Y. Wang acknowledges the Graduate Academy of Technische Universität Dresden for funding and S. Xing acknowledges the financial support *via* the China Scholarship Council (no. 201706070125).

References

1 Y. L. Wu, K. Fukuda, T. Yokota and T. Someya, *Adv. Mater.*, 2019, **31**, 1903687.
2 C. M. Lochner, Y. Khan, A. Pierre and A. C. Arias, *Nat. Commun.*, 2014, **5**, 5745.
3 Y. Khan, D. Han, A. Pierre, J. Ting, X. Wang, C. M. Lochner, G. Bovo, N. Yaacobi-Gross, C. Newsome, R. Wilson and A. C. Arias, *Proc. Natl. Acad. Sci. U. S. A.*, 2018, **115**, E11015–E11024.
4 Y. Wang, J. Benduhn, L. Baisinger, C. Lungenschmied, K. Leo and D. Spoltore, *ACS Appl. Mater. Interfaces*, 2021, **13**, 23239–23246.
5 M. Babics, H. Bristow, W. Zhang, A. Wadsworth, M. Neophytou, N. Gasparini and I. McCulloch, *J. Mater. Chem. C*, 2021, **9**, 2375–2380.
6 P. C. Y. Chow and T. Someya, *Adv. Mater.*, 2020, **32**, 1902045.
7 J. J. Kim, Y. Wang, H. Wang, S. Lee, T. Yokota and T. Someya, *Adv. Funct. Mater.*, 2021, 2009602.
8 C. Fuentes-Hernandez, W. F. Chou, T. M. Khan, L. Diniz, J. Lukens, F. A. Larrain, V. A. Rodriguez-Toro and B. Kippelen, *Science*, 2020, **370**, 698–701.
9 X. Xu, X. Zhou, K. Zhou, Y. Xia, W. Ma and O. Inganäs, *Adv. Funct. Mater.*, 2018, **28**, 1805570.
10 M. Heuken and N. Meyer, *Org. Electron. Mater. Manuf. Appl.*, 2006, **10**, 203–232.
11 F. C. Krebs, *Sol. Energy Mater. Sol. Cells*, 2009, **93**, 465–475.
12 C. Girotto, D. Moia, B. P. Rand and P. Heremans, *Adv. Funct. Mater.*, 2011, **21**, 64–72.
13 D. Li and L. J. Guo, *Appl. Phys. Lett.*, 2006, **88**, 063513.
14 Y. Xia, L. E. Aguirre, X. Xu and O. Inganäs, *Adv. Electron. Mater.*, 2020, **6**, 1901017.
15 A. J. P. Theuwissen, *Solid State Electron.*, 2008, **52**, 1401–1406.
16 X. Gong, M. Tong, Y. Xia, W. Cai, J. S. Moon, Y. Cao, G. Yu, C. L. Shieh, B. Nilsson and A. J. Heeger, *Science*, 2009, **325**, 1665–1667.
17 F. Verstraeten, S. Gielen, P. Verstappen, J. Raymakers, H. Penxten, L. Lutsen, K. Vandewal and W. Maes, *J. Mater. Chem. C*, 2020, **8**, 10098–10103.
18 J. Yang, J. Huang, R. Li, H. Li, B. Sun, Q. Lin, M. Wang, Z. Ma, K. Vandewal and Z. Tang, *Chem. Mater.*, 2021, **33**, 5147–5155.
19 W. Li, H. Guo, Z. Wang and G. Dong, *J. Phys. Chem. C*, 2017, **121**, 15333–15338.
20 W. Li, D. Li, G. Dong, L. Duan, J. Sun, D. Zhang and L. Wang, *Laser Photonics Rev.*, 2016, **10**, 473–480.
21 D. M. Lyons, A. Armin, M. Stolterfoht, R. C. R. Nagiri, R. D. Jansen-Van Vuuren, B. N. Pal, P. L. Burn, S. C. Lo and P. Meredith, *Org. Electron.*, 2014, **15**, 2903–2911.
22 H. Zhang, S. Jenatsch, J. De Jonghe, F. Nuësch, R. Steim, A. C. Véron and R. Hany, *Sci. Rep.*, 2015, **5**, 9439.
23 T. P. Osedach, A. Iacchetti, R. R. Lunt, T. L. Andrew, P. R. Brown, G. M. Akselrod and V. Bulović, *Appl. Phys. Lett.*, 2012, **101**, 113303.
24 A. Armin, R. D. J. Vuuren, N. Kopidakis, P. L. Burn and P. Meredith, *Nat. Commun.*, 2015, **6**, 6343.
25 W. Wang, F. Zhang, M. Du, L. Li, M. Zhang, K. Wang, Y. Wang, B. Hu, Y. Fang and J. Huang, *Nano Lett.*, 2017, **17**, 1995–2002.
26 B. Xie, R. Xie, K. Zhang, Q. Yin, Z. Hu, G. Yu, F. Huang and Y. Cao, *Nat. Commun.*, 2020, **11**, 2871.

27 B. Siegmund, A. Mischok, J. Benduhn, O. Zeika, S. Ullbrich, F. Nehm, M. Böhm, D. Spoltore, H. Fröb, C. Körner, K. Leo and K. Vandewal, *Nat. Commun.*, 2017, **8**, 15421.

28 Y. Lin, M. I. Nugraha, Y. Firdaus, A. D. Scaccabarozzi, F. Aniés, A. H. Emwas, E. Yengel, X. Zheng, J. Liu, W. Wahyudi, E. Yarali, H. Faber, O. M. Bakr, L. Tsetseris, M. Heeney and T. D. Anthopoulos, *ACS Energy Lett.*, 2020, **5**, 3663–3671.

29 Y. Lin, Y. Firdaus, F. H. Isikgor, M. I. Nugraha, E. Yengel, G. T. Harrison, R. Hallani, A. El-Labban, H. Faber, C. Ma, X. Zheng, A. Subbiah, C. T. Howells, O. M. Bakr, I. McCulloch, S. De Wolf, L. Tsetseris and T. D. Anthopoulos, *ACS Energy Lett.*, 2020, **5**, 2935–2944.

30 Y. Cui, H. Yao, J. Zhang, K. Xian, T. Zhang, L. Hong, Y. Wang, Y. Xu, K. Ma, C. An, C. He, Z. Wei, F. Gao and J. Hou, *Adv. Mater.*, 2020, **32**, 1908205.

31 Y. Cai, Y. Li, R. Wang, H. Wu, Z. Chen, J. Zhang, Z. Ma, X. Hao, Y. Zhao, C. Zhang, F. Huang and Y. Sun, *Adv. Mater.*, 2021, **33**, 2101733.

32 J. Lee, S. J. Ko, H. Lee, J. Huang, Z. Zhu, M. Seifrid, J. Vollbrecht, V. V. Brus, A. Karki, H. Wang, K. Cho, T. Q. Nguyen and G. C. Bazan, *ACS Energy Lett.*, 2019, **4**, 1401–1409.

33 W. Peng, Y. Liu, C. Wang, R. Hu, J. Zhang, D. Xu and Y. Wang, *J. Mater. Chem. C*, 2015, **3**, 5073.

34 R. Reuter and H. Franke, *Appl. Phys. B: Photophys. Laser Chem.*, 1989, **48**, 219–224.

35 J. H. Vella, L. Huang, N. Eedugurala, K. S. Mayer, T. N. Ng and J. D. Azoulay, *Sci. Adv.*, 2021, **7**, eabg2418.

36 M. Daanoune, R. Clerc, B. Flament and L. Hirsch, *J. Appl. Phys.*, 2020, **127**, 055502.

37 S. M. Sze and L. K. Ng, *Physics of Semiconductor Devices*, John Wiley & Sons, 3rd edn, 2006.

38 G. Konstantatos, I. Howard, A. Fischer, S. Hoogland, J. Clifford, E. Klem, L. Levina and E. H. Sargent, *Nature*, 2006, **442**, 180–183.

39 S. R. Forrest, *Nature*, 2004, **428**, 911–918.

40 K. Walzer, B. Männig, M. Pfeiffer and K. Leo, *Chem. Rev.*, 2007, **107**, 1233–1271.

41 A. Tsumura, H. Koezuka and T. Ando, *Appl. Phys. Lett.*, 1986, **49**, 1210–1212.

42 B. Lucas, T. Trigaud and C. Videlot-Ackermann, *Polym. Int.*, 2012, **61**, 374–389.

43 B. Yang, Y. Wang, L. Li, J. Zhang, J. Wang, H. Jiao, D. Hao, P. Guo, S. Zeng, Z. Hua and J. Huang, *Adv. Funct. Mater.*, 2021, 2103787.

44 D. Q. Tan, *Adv. Funct. Mater.*, 2020, **30**, 1808567.

45 H. Ren, J. De Chen, Y. Q. Li and J. X. Tang, *Adv. Sci.*, 2021, **8**, 2002418.

46 J. Reynaert, V. I. Arkhipov, P. Heremans and J. Poortmans, *Adv. Funct. Mater.*, 2006, **16**, 784–790.

47 M. Hiramoto, T. Imahigashi and M. Yokoyama, *Appl. Phys. Lett.*, 1994, **64**, 187–189.

48 W. T. Hammond, J. P. Mudrick and J. Xue, *J. Appl. Phys.*, 2014, **116**, 214501.

49 R. Nie, X. Deng, L. Feng, G. Hu, Y. Wang, G. Yu and J. Xu, *Small*, 2017, **13**, 1603260.

50 J. Huang, J. Lee, M. Schrock, A. L. Dixon, A. T. Lill, K. Cho, G. C. Bazan and T. Q. Nguyen, *Mater. Horiz.*, 2020, **7**, 3234.

51 T. Katsume, M. Hiramoto and M. Yokoyama, *Appl. Phys. Lett.*, 1996, **69**, 3722–3724.

52 H. Rost and H. H. Hörhold, *Phys. Rev. B: Condens. Matter Mater. Phys.*, 1999, **59**, 1964–1972.

53 G. Matsunobu, Y. Oishi, M. Yokoyama and M. Hiramoto, *Appl. Phys. Lett.*, 2002, **81**, 1321–1322.

54 F. C. Chen, S. C. Chien and G. L. Cious, *Appl. Phys. Lett.*, 2010, **97**, 103301.

55 R. Dong, C. Bi, Q. Dong, F. Guo, Y. Yuan, Y. Fang, Z. Xiao and J. Huang, *Adv. Opt. Mater.*, 2014, **2**, 549–554.

56 L. Shen, Y. Fang, Q. Dong, Z. Xiao and J. Huang, *Appl. Phys. Lett.*, 2015, **106**, 023301.

57 X. Li, X. Li, S. Wang and Y. Xiao, *J. Mater. Chem. C*, 2016, **4**, 5584.

58 L. Li, F. Zhang, J. Wang, Q. An, Q. Sun, W. Wang, J. Zhang and F. Teng, *Sci. Rep.*, 2015, **5**, 9181.

59 L. Li, F. Zhang, W. Wang, Y. Fang and J. Huang, *Phys. Chem. Chem. Phys.*, 2015, **17**, 30712.

60 J. Huang and Y. Yang, *Appl. Phys. Lett.*, 2007, **91**, 203505.

61 Y. Fang, F. Guo, Z. Xiao and J. Huang, *Adv. Opt. Mater.*, 2014, **2**, 348–353.

62 J. W. Lee, D. Y. Kim and F. So, *Adv. Funct. Mater.*, 2015, **25**, 1233–1238.

63 W. T. Hammond and J. Xue, *Appl. Phys. Lett.*, 2010, **97**, 073302.

64 D. Yang, X. Zhou, Y. Wang, A. Vadim, S. M. Alshehri, T. Ahamad and D. Ma, *J. Mater. Chem. C*, 2016, **4**, 2160.

65 Z. Zhao, C. Xu, L. Niu, X. Zhang and F. Zhang, *Laser Photonics Rev.*, 2020, **14**, 2000262.

66 P. Peumans, A. Yakimov and S. R. Forrest, *J. Appl. Phys.*, 2003, **93**, 3693–3723.

67 O. V. Mikhnenko, P. W. M. Blom and T. Q. Nguyen, *Energy Environ. Sci.*, 2015, **8**, 1867.

68 C. W. Tang, *Appl. Phys. Lett.*, 1986, **48**, 183–185.

69 G. Yu, J. Gao, J. C. Hummelen, F. Wudl and A. J. Heeger, *Science*, 1995, **270**, 1789–1791.

70 J. J. M. Halls, C. A. Walsh, N. C. Greenham, E. A. Marseglia, R. H. Friend, S. C. Morattlt and A. B. Holmes, *Nature*, 1995, **376**, 498–500.

71 X. Ren, F. Yang, X. Gao, S. Cheng, X. Zhang, H. Dong and W. Hu, *Adv. Energy Mater.*, 2018, **8**, 1801223.

72 M. G. Han, K. B. Park, X. Bulliard, G. H. Lee, S. Yun, D. S. Leem, C. J. Heo, T. Yagi, R. Sakurai, T. Ro, S. J. Lim, S. Sul, K. Na, J. Ahn, Y. W. Jin and S. Lee, *ACS Appl. Mater. Interfaces*, 2016, **8**, 26143–26151.

73 Z. Lan, Y. S. Lau, Y. Wang, Z. Xiao, L. Ding, D. Luo and F. Zhu, *Adv. Opt. Mater.*, 2020, 2001388.

74 Z. Tang, Z. Ma, A. Sánchez-Díaz, S. Ullbrich, Y. Liu, B. Siegmund, A. Mischok, K. Leo, M. Campoy-Quiles, W. Li and K. Vandewal, *Adv. Mater.*, 2017, **29**, 1702184.

75 S. Xing, V. C. Nikolis, J. Kublitski, E. Guo, X. Jia, Y. Wang, D. Spoltore, K. Vandewal, H. Kleemann, J. Benduhn and K. Leo, *Adv. Mater.*, 2021, 2102967.

76 R. Lukac, *J. Real-Time Image Process.*, 2006, **1**, 45–52.

77 S. Nishiwaki, T. Nakamura, M. Hiramoto, T. Fujii and M. A. Suzuki, *Nat. Photonics*, 2013, **7**, 240–246.

78 M. Dandin, P. Abshire and E. Smela, *Lab Chip*, 2007, **7**, 955–977.

79 Q. Lin, A. Armin, P. L. Burn and P. Meredith, *Nat. Photonics*, 2015, **9**, 687–694.

80 M. S. Ünlü and S. Strite, *J. Appl. Phys.*, 1995, **78**, 607–639.

81 J. Wang, S. Ullbrich, J. L. Hou, D. Spoltore, Q. Wang, Z. Ma, Z. Tang and K. Vandewal, *ACS Photonics*, 2019, **6**, 1393–1399.

82 Y. Wang, B. Siegmund, Z. Tang, Z. Ma, J. Kublitski, S. Xing, V. C. Nikolis, S. Ullbrich, Y. Li, J. Benduhn, D. Spoltore, K. Vandewal and K. Leo, *Adv. Opt. Mater.*, 2021, **9**, 2001784.

83 S. Xing, X. Wang, E. Guo, H. Kleemann and K. Leo, *ACS Appl. Mater. Interfaces*, 2020, **12**, 13061–13067.

84 J. L. Bredas, *AIP Conf. Proc.*, 2013, **1519**, 55–58.

85 A. Armin, W. Li, O. J. Sandberg, Z. Xiao, L. Ding, J. Nelson, D. Neher, K. Vandewal, S. Shoaee, T. Wang, H. Ade, T. Heumüller, C. Brabec and P. Meredith, *Adv. Energy Mater.*, 2021, **11**, 20003570.

86 M. L. Tietze, J. Benduhn, P. Pahner, B. Nell, M. Schwarze, H. Kleemann, M. Krammer, K. Zojer, K. Vandewal and K. Leo, *Nat. Commun.*, 2018, **9**, 1182.

87 A. Armin, M. Velusamy, P. Wolfer, Y. Zhang, P. L. Burn and P. Meredith, *ACS Photonics*, 2014, **1**, 173–181.

88 Q. D. Ou, Y. Q. Li and J. X. Tang, *Adv. Sci.*, 2016, **3**, 1–25.

89 Y. Park, K. Vandewal and K. Leo, *Small Methods*, 2018, **2**, 1800123.

90 D. E. Markov, J. C. Hummelen, P. W. M. Blom and A. B. Sieval, *Phys. Rev. B: Condens. Matter Mater. Phys.*, 2005, **72**, 045216.

91 J. J. M. Halls, K. Pichler and R. H. Friend, *J. Appl. Phys.*, 1996, **68**, 3120–3122.

92 W. A. Luhman and R. J. Holmes, *Adv. Funct. Mater.*, 2011, **21**, 764–771.

93 S. M. Menke and R. J. Holmes, *Energy Environ. Sci.*, 2014, **7**, 499–512.

94 Y. Terao, H. Sasabe and C. Adachi, *Appl. Phys. Lett.*, 2007, **90**, 1–3.

95 G. Wei, R. R. Lunt, K. Sun, S. Wang, M. E. Thompson and S. R. Forrest, *Nano Lett.*, 2010, **10**, 3555–3559.

96 T. Förster, *Discuss. Faraday Soc.*, 1959, **27**, 7–17.

97 D. L. Dexter, *J. Chem. Phys.*, 1953, **21**, 836–850.

98 G. D. Scholes, *Annu. Rev. Phys. Chem.*, 2003, **54**, 57–87.

99 R. Koeppe and N. S. Sariciftci, *Photochem. Photobiol. Sci.*, 2006, **5**, 1122–1131.

100 S. Raisys, K. Kazlauskas, M. Daskeviciene, T. Malinauskas, V. Getautis and S. Jursenas, *J. Mater. Chem. C*, 2014, **2**, 4792–4798.

101 R. R. Lunt, J. B. Benziger and S. R. Forrest, *Adv. Mater.*, 2010, **22**, 1233–1236.

102 S. M. Menke, W. A. Luhman and R. J. Holmes, *Nat. Mater.*, 2013, **12**, 152–157.

103 S. Athanasopoulos, E. Hennebicq, D. Beljonne and A. B. Walker, *J. Phys. Chem. C*, 2008, **112**, 11532–11538.

104 Y. Zhong, M. Causa', G. J. Moore, P. Krauspe, B. Xiao, F. Günther, J. Kublitski, R. Shivhare, J. Benduhn, E. BarOr, S. Mukherjee, K. M. Yallum, J. Réhault, S. C. B. Mannsfeld, D. Neher, L. J. Richter, D. M. DeLongchamp, F. Ortmann, K. Vandewal, E. Zhou and N. Banerji, *Nat. Commun.*, 2020, **11**, 833.

105 R. A. Marcus, *J. Phys. Chem.*, 1989, **93**, 3078–3086.

106 A. J. Ward, A. Ruseckas, M. M. Kareem, B. Ebenhoch, L. A. Serrano, M. Al-Eid, B. Fitzpatrick, V. M. Rotello, G. Cooke and I. D. W. Samuel, *Adv. Mater.*, 2015, **27**, 2496–2500.

107 T. M. Clarke and J. R. Durrant, *Chem. Rev.*, 2010, **110**, 6736–6767.

108 T. M. Clarke, A. M. Ballantyne, J. Nelson, D. D. C. Bradley and J. R. Durrant, *Adv. Funct. Mater.*, 2008, **18**, 4029–4035.

109 V. C. Nikolis, J. Benduhn, F. Holzmueller, F. Piersimoni, M. Lau, O. Zeika, D. Neher, C. Koerner, D. Spoltore and K. Vandewal, *Adv. Energy Mater.*, 2017, **7**, 1700855.

110 S. Liu, J. Yuan, W. Deng, M. Luo, Y. Xie, Q. Liang, Y. Zou, Z. He, H. Wu and Y. Cao, *Nat. Photonics*, 2020, **14**, 300–305.

111 R. Yu, H. Yao, Y. Cui, L. Hong, C. He and J. Hou, *Adv. Mater.*, 2019, **31**, 1902302.

112 E. T. Hoke, K. Vandewal, J. A. Bartelt, W. R. Mateker, J. D. Douglas, R. Noriega, K. R. Graham, J. M. J. Fréchet, A. Salleo and M. D. Mcgehee, *Adv. Energy Mater.*, 2013, **3**, 220–230.

113 G. Ren, C. W. Schlenker, E. Ahmed, S. Subramaniyan, S. Olthof, A. Kahn, D. S. Ginger and S. A. Jenekhe, *Adv. Funct. Mater.*, 2013, **23**, 1238–1249.

114 M. A. Faist, T. Kirchartz, W. Gong, R. S. Ashraf, I. McCulloch, J. C. De Mello, N. J. Ekins-Daukes, D. D. C. Bradley and J. Nelson, *J. Am. Chem. Soc.*, 2012, **134**, 685–692.

115 K. Vandewal, Z. Ma, J. Bergqvist, Z. Tang, E. Wang, P. Henriksson, K. Tvingstedt, M. R. Andersson and F. Zhang, *Adv. Funct. Mater.*, 2012, **22**, 3480–3490.

116 S. Westenhoff, I. A. Howard, J. M. Hodgkiss, K. R. Kirov, H. A. Bronstein, C. K. Williams, N. C. Greenham and R. H. Friend, *J. Am. Chem. Soc.*, 2008, **130**, 13653–13658.

117 C. W. Schlenker, K. S. Chen, H. L. Yip, C. Z. Li, L. R. Bradshaw, S. T. Ochsenbein, F. Ding, X. S. Li, D. R. Gamelin, A. K. Y. Jen and D. S. Ginger, *J. Am. Chem. Soc.*, 2012, **134**, 19661–19668.

118 J. Benduhn, F. Piersimoni, G. Londi, A. Kirch, J. Widmer, C. Koerner, D. Beljonne, D. Neher, D. Spoltore and K. Vandewal, *Adv. Energy Mater.*, 2018, **8**, 1800451.

119 J. L. Brédas, D. Beljonne, V. Coropceanu and J. Cornil, *Chem. Rev.*, 2004, **104**, 4971–5003.

120 K. Vandewal, S. Albrecht, E. T. Hoke, K. R. Graham, J. Widmer, J. D. Douglas, M. Schubert, W. R. Mateker, J. T. Bloking, G. F. Burkhard, A. Sellinger, J. M. J. Fréchet, A. Amassian, M. K. Riede, M. D. McGehee, D. Neher and A. Salleo, *Nat. Mater.*, 2014, **13**, 63–68.

121 K. Vandewal, *Annu. Rev. Phys. Chem.*, 2016, **67**, 113–133.

122 A. A. Bakulin, A. Rao, V. G. Pavelyew, P. H. M. van Loos-dRecht, M. S. Pshenichnikov, D. Niedzialek, J. Cornil, D. Beljonne and R. H. Friend, *Science*, 2012, **335**, 1340–1344.

123 H. Tamura and I. Burghardt, *J. Am. Chem. Soc.*, 2013, **135**, 16364–16367.

124 A. A. Paraecattil and N. Banerji, *J. Am. Chem. Soc.*, 2014, **136**, 1472–1482.

125 W. Warta and N. Karl, *Phys. Rev. B: Condens. Matter Mater. Phys.*, 1985, **32**, 1172–1182.

126 W. Warta, R. Stehle and N. Karl, *Appl. Phys. A: Mater. Sci. Process.*, 1985, **36**, 163–170.

127 Y. Yuan, G. Giri, A. L. Ayzner, A. P. Zoombelt, S. C. B. Mannsfeld, J. Chen, D. Nordlund, M. F. Toney, J. Huang and Z. Bao, *Nat. Commun.*, 2014, **5**, 3005.

128 D. Ji, T. Li, J. Liu, S. Amirjalayer, M. Zhong, Z. Y. Zhang, X. Huang, Z. Wei, H. Dong, W. Hu and H. Fuchs, *Nat. Commun.*, 2019, **10**, 12.

129 H. Bässler and A. Köhler, Charge Transport in Organic Semiconductors, in *Unimolecular and Supramolecular Electronics I*, ed. R. Metzger, Topics in Current Chemistry, 2011, vol. 312, Springer, Berlin, Heidelberg.

130 N. B. Kotadiya, A. Mondal, P. W. M. Blom, D. Andrienko and G. J. A. H. Wetzelaer, *Nat. Mater.*, 2019, **18**, 1182–1186.

131 R. Noriega, J. Rivnay, K. Vandewal, F. P. V. Koch, N. Stingelin, P. Smith, M. F. Toney and A. Salleo, *Nat. Mater.*, 2013, **12**, 1038–1044.

132 K. Vandewal, K. Tvingstedt, A. Gadisa, O. Inganäs and J. V. Manca, *Phys. Rev. B: Condens. Matter Mater. Phys.*, 2010, **81**, 1–8.

133 U. Rau, *Phys. Rev. B: Condens. Matter Mater. Phys.*, 2007, **76**, 1–8.

134 K. Vandewal, J. Widmer, T. Heumueller, C. J. Brabec, M. D. McGehee, K. Leo, M. Riede and A. Salleo, *Adv. Mater.*, 2014, **26**, 3839–3843.

135 J. Benduhn, K. Tvingstedt, F. Piersimoni, S. Ullbrich, Y. Fan, M. Tropiano, K. A. McGarry, O. Zeika, M. K. Riede, C. J. Douglas, S. Barlow, S. R. Marder, D. Neher, D. Spoltore and K. Vandewal, *Nat. Energy*, 2017, **2**, 17053.

136 J. Kublitski, A. Hofacker, B. K. Boroujeni, J. Benduhn, V. C. Nikolis, C. Kaiser, D. Spoltore, H. Kleemann, A. Fischer, F. Ellinger, K. Vandewal and K. Leo, *Nat. Commun.*, 2021, **12**, 551.

137 G. Simone, M. J. Dyson, S. C. J. Meskers, R. A. J. Janssen and G. H. Gelinck, *Adv. Funct. Mater.*, 2020, **30**, 1904205.

138 S. Gielen, C. Kaiser, F. Verstraeten, J. Kublitski, J. Benduhn, D. Spoltore, P. Verstappen, W. Maes, P. Meredith, A. Armin and K. Vandewal, *Adv. Mater.*, 2020, **32**, 2003818.

139 M. Azzouzi, J. Yan, T. Kirchartz, K. Liu, J. Wang, H. Wu and J. Nelson, *Phys. Rev. X*, 2018, **8**, 031055.

140 C. C. Lee, S. Biring, S. J. Ren, Y. Z. Li, M. Z. Li, N. R. Al Amin and S. W. Liu, *Org. Electron.*, 2019, **65**, 150–155.

141 S. Yoon, J. Ha, J. Cho and D. S. Chung, *Adv. Opt. Mater.*, 2016, **4**, 1933–1938.

142 H. Shekhar, O. Solomeshch, D. Liraz and N. Tessler, *Appl. Phys. Lett.*, 2017, **111**, 223301.

143 T. Agostinelli, M. Campoy-Quiles, J. C. Blakesley, R. Speller, D. D. C. Bradley and J. Nelson, *Appl. Phys. Lett.*, 2008, **93**, 203305.

144 H. Wang, S. Xing, Y. Zheng, J. Kong, J. Yu and A. D. Taylor, *ACS Appl. Mater. Interfaces*, 2018, **10**, 3856–3864.

145 L. Groenendaal, F. Jonas, D. Freitag, H. Pielartzik and J. R. Reynolds, *Adv. Mater.*, 2000, **12**, 481–494.

146 M. Kielar, O. Dhez, G. Pecastaings, A. Curutchet and L. Hirsch, *Sci. Rep.*, 2016, **6**, 39201.

147 Y. Zhou, C. Fuentes-hernandez, J. Shim, J. Meyer, A. J. Giordano, H. Li, P. Winget, T. Papadopoulos, H. Cheun, J. Kim, M. Fenoll, A. Dindar, W. Haske, E. Najafabadi, T. M. Khan, H. Sojoudi, S. Barlow, S. Graham, J. Brédas, S. R. Marder, A. Kahn and B. Kippelen, *Science*, 2012, **873**, 327–332.

148 M. S. White, D. C. Olson, S. E. Shaheen, N. Kopidakis and D. S. Ginley, *Appl. Phys. Lett.*, 2006, **89**, 143517.

149 Y. Zheng, A. Fischer, N. Sergeeva, S. Reineke and S. C. B. Mannsfeld, *Org. Electron.*, 2019, **65**, 82–90.

150 C. Jonda, A. B. R. Mayer, U. Stolz, A. Elschner and A. Karbach, *J. Mater. Sci.*, 2000, **35**, 5645–5651.

151 K. Fostiropoulos, M. Vogel, B. Mertesacker and A. Weidinger, *Org. Photovoltaics III*, 2003, **4801**, 1–6.

152 B. Friedel, P. E. Keivanidis, T. J. K. Brenner, A. Abrusci, C. R. McNeill, R. H. Friend and N. C. Greenham, *Macromolecules*, 2009, **42**, 6741–6747.

153 G. A. M. Hurkx, D. B. M. Klaassen and M. P. G. Knuvers, *IEEE Trans. Electron Devices*, 1992, **39**, 331–338.

154 B. Bouthinon, R. Clerc, J. Vaillant, J. M. Verilhac, J. Faure-Vincent, D. Djurado, I. Ionica, G. Man, A. Gras, G. Pananakakis, R. Gwoziecki and A. Kahn, *Adv. Funct. Mater.*, 2015, **25**, 1090–1101.

155 A. H. Fallahpour, S. Kienitz and P. Lugli, *IEEE Trans. Electron Devices*, 2017, **64**, 2649–2654.

156 N. Zarrabi, O. J. Sandberg, S. Zeiske, W. Li, D. B. Riley, P. Meredith and A. Armin, *Nat. Commun.*, 2020, **11**, 5567.

157 G. Simone, M. J. Dyson, C. H. L. Weijtens, S. C. J. Meskers, R. Coehoorn, R. A. J. Janssen and G. H. Gelinck, *Adv. Opt. Mater.*, 2020, **8**, 1901568.

158 R. D. Jansen-van Vuuren, A. Armin, A. K. Pandey, P. L. Burn and P. Meredith, *Adv. Mater.*, 2016, **28**, 4766–4802.

159 S. Saggar, S. Sanderson, D. Gedefaw, X. Pan, B. Philippa, M. R. Andersson, S.-C. Lo and E. B. Namdas, *Adv. Funct. Mater.*, 2021, 2010661.

160 S. Ullbrich, B. Siegmund, A. Mischok, A. Hofacker, J. Benduhn, D. Spoltore and K. Vandewal, *J. Phys. Chem. Lett.*, 2017, **8**, 5621–5625.

161 J. Miao and F. Zhang, *Laser Photonics Rev.*, 2019, **13**, 1800204.

162 K. I. Nakayama, M. Hiramoto and M. Yokoyama, *Appl. Phys. Lett.*, 2000, **76**, 1194–1196.

163 M. Hiramoto, A. Miki, M. Yoshida and M. Yokoyama, *Appl. Phys. Lett.*, 2002, **81**, 1500–1502.

164 T. Hahn, S. Tscheuschner, F. J. Kahle, M. Reichenberger, S. Athanasopoulos, C. Saller, G. C. Bazan, T. Q. Nguyen, P. Strohriegl, H. Bässler and A. Köhler, *Adv. Funct. Mater.*, 2017, **27**, 1604906.

165 H. Yu, R. Yi, J. Zhang, A. Yu, H. Peng, J. Qin and X. Hou, *J. Phys. D: Appl. Phys.*, 2016, **49**, 205105.

166 J. Euvrard, A. Revaux, A. Kahn and D. Vuillaume, *Org. Electron.*, 2020, **76**, 105450.

167 C. M. Proctor, S. Albrecht, M. Kuik, D. Neher and T. Q. Nguyen, *Adv. Energy Mater.*, 2014, **4**, 1400230.

168 M. C. Scharber, M. Koppe, J. Gao, F. Cordella, M. A. Loi, P. Denk, M. Morana, H. J. Egelhaaf, K. Forberich, G. Dennler, R. Gaudiana, D. Waller, Z. Zhu, X. Shi and C. J. Brabec, *Adv. Mater.*, 2010, **22**, 367–370.

169 P. Hartnagel and T. Kirchartz, *Adv. Theory Simul.*, 2020, **3**, 2000116.

170 T. Rauch, M. Böberl, S. F. Tedde, J. Fürst, M. V. Kovalenko, G. Hesser, U. Lemmer, W. Heiss and O. Hayden, *Nat. Photonics*, 2009, **3**, 332–336.

171 T. N. Ng, W. S. Wong, M. L. Chabinyc, S. Sambandan and R. A. Street, *Appl. Phys. Lett.*, 2008, **92**, 213303.

172 D. Baierl, L. Pancheri, M. Schmidt, D. Stoppa, G. F. Dalla Betta, G. Scarpa and P. Lugli, *Nat. Commun.*, 2012, **3**, 1175.

173 H. Shekhar, A. Fenigstein, T. Leitner, B. Lavi, D. Veinger and N. Tessler, *Sci. Rep.*, 2020, **10**, 7594.

174 Y. Lee, J. Y. Oh, W. Xu, O. Kim, T. R. Kim, J. Kang, Y. Kim, D. Son, J. B. H. Tok, M. J. Park, Z. Bao and T. W. Lee, *Sci. Adv.*, 2018, **4**, eaat7387.

175 J. H. Kim, A. Liess, M. Stolte, A. Krause, V. Stepanenko, C. Zhong, D. Bialas, F. Spano and F. Würthner, *Adv. Mater.*, 2021, **33**, 2100582.

176 B. Sun, G. Zhou, Y. Wang, X. Xu, L. Tao, N. Zhao, H. K. Tsang, X. Wang, Z. Chen and J. Xu, *Adv. Opt. Mater.*, 2021, 2100158.

177 A. Liess, A. Arjona-Esteban, A. Kudzus, J. Albert, A. M. Krause, A. Lv, M. Stolte, K. Meerholz and F. Würthner, *Adv. Funct. Mater.*, 2019, **29**, 1805058.

178 R. D. Jansen-Van Vuuren, A. Pivrikas, A. K. Pandey and P. L. Burn, *J. Mater. Chem. C*, 2013, **1**, 3532–3543.

179 K. Xia, Y. Li, Y. Wang, L. Portilla and V. Pecunia, *Adv. Opt. Mater.*, 2020, **8**, 1902056.

180 S. Z. Hassan, H. J. Cheon, C. Choi, S. Yoon, M. Kang, J. Cho, Y. H. Jang, S. K. Kwon, D. S. Chung and Y. H. Kim, *ACS Appl. Mater. Interfaces*, 2019, **11**, 28106–28114.

181 H. Opoku, B. Lim, E. S. Shin, H. Kong, J. M. Park, C. Bathula and Y. Y. Noh, *Macromol. Chem. Phys.*, 2019, **220**, 1900287.

182 J. Y. Kim, P. Vincent, J. Jang, M. S. Jang, M. Choi, J. H. Bae, C. Lee and H. Kim, *J. Alloys Compd.*, 2020, **813**, 152202.

183 J. Kang, J. Kim, H. Ham, H. Ahn, S. Y. Lim, H. M. Kim, I. N. Kang and I. H. Jung, *Adv. Opt. Mater.*, 2020, **8**, 2001038.

184 T. Schembri, J. H. Kim, A. Liess, V. Stepanenko, M. Stolte and F. Würthner, *Adv. Opt. Mater.*, 2021, 2100213.

185 K. H. Lee, D. S. Leem, J. S. Castrucci, K. B. Park, X. Bulliard, K. S. Kim, Y. W. Jin, S. Lee, T. P. Bender and S. Y. Park, *ACS Appl. Mater. Interfaces*, 2013, **5**, 13089–13095.

186 H. O. Toshikatsu Sakai, H. Seo and T. Takagi, *MRS Adv.*, 2015, **1**, 459–464.

187 S. J. Lim, D. S. Leem, K. B. Park, K. S. Kim, S. Sul, K. Na, G. H. Lee, C. J. Heo, K. H. Lee, X. Bulliard, R. I. Satoh, T. Yagi, T. Ro, D. Im, J. Jung, M. Lee, T. Y. Lee, M. G. Han, Y. W. Jin and S. Lee, *Sci. Rep.*, 2015, **5**, 7708.

188 W. Li, S. Li, L. Duan, H. Chen, L. Wang, G. Dong and Z. Xu, *Org. Electron.*, 2016, **37**, 346–351.

189 C. W. Joo, J. Kim, J. Moon, K. M. Lee, J. E. Pi, S. Y. Kang, S. D. Ahn, Y. S. Park and D. S. Chung, *Org. Electron.*, 2019, **70**, 101–106.

190 G. H. Lee, X. Bulliard, S. Yun, D.-S. Leem, K.-B. Park, K.-H. Lee, C.-J. Heo, I.-S. Jung, J.-H. Kim, Y. S. Choi, S.-J. Lim and Y. W. Jin, *Opt. Express*, 2019, **27**, 25410–25419.

191 D. Shen, Z. Guan, M. Li, S.-W. Tsang, W. Zhang, M.-F. Lo and C.-S. Lee, *J. Mater. Chem. C*, 2021, **9**, 3814.

192 A. Yazmaciyan, P. Meredith and A. Armin, *Adv. Opt. Mater.*, 2019, **7**, 1801543.

193 W. Wang, M. Du, M. Zhang, J. Miao, Y. Fang and F. Zhang, *Adv. Opt. Mater.*, 2018, **6**, 1800249.

194 T. Y. Li, T. Meyer, Z. Ma, J. Benduhn, C. Korner, O. Zeika, K. Vandewal and K. Leo, *J. Am. Chem. Soc.*, 2017, **139**, 13636–13639.

195 J. Huang, J. Lee, H. Nakayama, M. Schrock, D. X. Cao, K. Cho, G. C. Bazan and T. Q. Nguyen, *ACS Nano*, 2021, **15**, 1753–1763.

196 J. D. Zimmerman, E. K. Yu, V. V. Diev, K. Hanson, M. E. Thompson and S. R. Forrest, *Org. Electron.*, 2011, **12**, 869–873.

197 C. Kaiser, K. S. Schellhammer, J. Benduhn, B. Siegmund, M. Tropiano, J. Kublitski, D. Spoltore, M. Panhans, O. Zeika, F. Ortmann, P. Meredith, A. Armin and K. Vandewal, *Chem. Mater.*, 2019, **31**, 9325–9330.

198 A. Mischok, B. Siegmund, D. S. Ghosh, J. Benduhn, D. Spoltore, M. Böhm, H. Fröb, C. Körner, K. Leo and K. Vandewal, *ACS Photonics*, 2017, **4**, 2228–2234.

199 X. Tang, M. M. Ackerman, M. Chen and P. Guyot-Sionnest, *Nat. Photonics*, 2019, **13**, 277–282.

200 Z. Lan, Y. Lei, W. K. E. Chan, S. Chen, D. Luo and F. Zhu, *Sci. Adv.*, 2020, **6**, eaaw8065.

201 J. Kublitski, A. Fischer, S. Xing, L. Baisinger, E. Bittrich, D. Spoltore, J. Benduhn, K. Vandewal and K. Leo, *Nat. Commun.*, 2021, **12**, 4259.

202 A. Pierre, I. Deckman, P. B. Lechêne and A. C. Arias, *Adv. Mater.*, 2015, **27**, 6411–6417.

203 A. Armin, M. Hambsch, I. K. Kim, P. L. Burn, P. Meredith and E. B. Namdas, *Laser Photonics Rev.*, 2014, **8**, 924–932.

204 Y. Wei, Z. Ren, A. Zhang, P. Mao, H. Li, X. Zhong, W. Li, S. Yang and J. Wang, *Adv. Funct. Mater.*, 2018, **28**, 1706690.

205 E. Saracco, B. Bouthinon, J. M. Verilhac, C. Celle, N. Chevalier, D. Mariolle, O. Dhez and J. P. Simonato, *Adv. Mater.*, 2013, **25**, 6534–6538.

206 Z. Zhong, K. Li, J. Zhang, L. Ying, R. Xie, G. Yu, F. Huang and Y. Cao, *ACS Appl. Mater. Interfaces*, 2019, **11**, 14208–14214.

207 X. Zhou, D. Yang and D. Ma, *Adv. Opt. Mater.*, 2015, **3**, 1570–1576.

208 L. Xiao, S. Chen, X. Chen, X. Peng, Y. Cao and X. Zhu, *J. Mater. Chem. C*, 2018, **6**, 3341.

209 Z. Huang, Z. Zhong, F. Peng, L. Ying, G. Yu, F. Huang and Y. Cao, *ACS Appl. Mater. Interfaces*, 2021, **13**, 1027–1034.

210 F. Guo, Z. Xiao and J. Huang, *Adv. Opt. Mater.*, 2013, **1**, 289–294.

211 C. C. Lee, R. Estrada, Y. Z. Li, S. Biring, N. R. Al Amin, M. Z. Li, S. W. Liu and K. T. Wong, *Adv. Opt. Mater.*, 2020, **8**, 2000519.

212 L. Shen, Y. Fang, H. Wei, Y. Yuan and J. Huang, *Adv. Mater.*, 2016, **28**, 2043–2048.

213 M. Liu, J. Wang, Z. Zhao, K. Yang, P. Durand, F. Ceugniet, G. Ulrich, L. Niu, Y. Ma, N. Leclerc, X. Ma, L. Shen and F. Zhang, *J. Phys. Chem. Lett.*, 2021, **12**, 2937–2943.

214 X. Zhang, E. Zheng, M. R. Esopi, C. Cai and Q. Yu, *ACS Appl. Mater. Interfaces*, 2018, **10**, 24064–24074.

215 F. C. Krebs, M. Biancardo, B. Winther-Jensen, H. Spanggard and J. Alstrup, *Sol. Energy Mater. Sol. Cells*, 2006, **90**, 1058–1067.

216 R. Eckstein, T. Rödlmeier, T. Glaser, S. Valouch, R. Mauer, U. Lemmer and G. Hernandez-Sosa, *Adv. Electron. Mater.*, 2015, **1**, 1500101.

217 J. Zhong, X. Wu, S. Lan, Y. Fang, H. Chen and T. Guo, *ACS Photonics*, 2018, **5**, 3712–3722.

218 K. Xu, Y. Lu and K. Takei, *Adv. Mater. Technol.*, 2019, **4**, 1800628.

219 J. Huang, J. Lee, J. Vollbrecht, V. V. Brus, A. L. Dixon, D. X. Cao, Z. Zhu, Z. Du, H. Wang, K. Cho, G. C. Bazan and T. Q. Nguyen, *Adv. Mater.*, 2020, **32**, 1906027.

220 Y. Khan, C. M. Lochner, A. Pierre and A. C. Arias, *Proc. - 2015 6th IEEE Int. Work. Adv. Sensors Interfaces, IWASI 2015*, 2015, 83–86.

221 G. Yu, J. Wang, J. McElvain and A. J. Heeger, *Adv. Mater.*, 1998, **10**, 1431–1434.

222 P. Büchele, M. Richter, S. F. Tedde, G. J. Matt, G. N. Ankah, R. Fischer, M. Biele, W. Metzger, S. Lilliu, O. Bikondoa, J. E. Macdonald, C. J. Brabec, T. Kraus, U. Lemmer and O. Schmidt, *Nat. Photonics*, 2015, **9**, 843–848.

223 X. Xu, M. Davanco, X. Qi and S. R. Forrest, *Org. Electron.*, 2008, **9**, 1122–1127.

224 T. Yokota, T. Nakamura, H. Kato, M. Mochizuki, M. Tada, M. Uchida, S. Lee, M. Koizumi, W. Yukita, A. Takimoto and T. Someya, *Nat. Electron.*, 2020, **3**, 113–121.

225 L. Duan and A. Uddin, *Adv. Sci.*, 2020, **7**, 1903259.

226 Y. Fang, A. Armin, P. Meredith and J. Huang, *Nat. Photonics*, 2019, **13**, 1–4.

227 G. H. Rieke, *Detection of Light*, Cambridge University Press, 3rd edn, 2021.

228 R. Müller, *Generation-Recombination Noise*, Springer Berlin Heidelberg, Berlin, Heidelberg, 1978.

229 J. Cohen, *NBS Technical Note 1173: Three Guises of Generation-Recombination Noise*, Washington, D.C., 1983.

230 A. Rogalski, *Infrared Detectors*, CRC Press, 2nd edn, 2010.

231 K. A. Luck, V. K. Sangwan, P. E. Hartnett, H. N. Arnold, M. R. Wasielewski, T. J. Marks and M. C. Hersam, *Adv. Funct. Mater.*, 2017, **27**, 1703805.

232 R. C. Jones, *Rev. Sci. Instrum.*, 1953, **24**, 1035–1040.

233 F. Stöckmann, *Appl. Phys.*, 1975, **7**, 1–5.

234 A. Pierre, A. Gaikwad and A. C. Arias, *Nat. Photonics*, 2017, **11**, 193–199.

235 L. Shen, Y. Zhang, Y. Bai, X. Zheng, Q. Wang and J. Huang, *Nanoscale*, 2016, **8**, 12990.

236 S. G. Chamberlain and J. P. Y. Lee, *IEEE J. Solid-State Circuits*, 1984, **19**, 41–48.

237 C. Xie and F. Yan, *Small*, 2017, **13**, 1701822.

238 A. Altaqui, P. Sen, H. Schrickx, J. Rech, J. W. Lee, M. Escuti, W. You, B. J. Kim, R. Kolbas, B. T. O'Connor and M. Kudenov, *Sci. Adv.*, 2021, **7**, eabe3196.

239 S. Schubert, L. Müller-Meskamp and K. Leo, *Adv. Funct. Mater.*, 2014, **24**, 6668–6676.

240 S. Schubert, J. Meiss, L. Müller-Meskamp and K. Leo, *Adv. Energy Mater.*, 2013, **3**, 438–443.

241 X. Gong, M. H. Tong, S. H. Park, M. Liu, A. Jen and A. J. Heeger, *Sensors*, 2010, **10**, 6488–6496.